



Estimating monthly global ground-level NO₂ concentrations using geographically weighted panel regression



Chao Li, Shunsuke Managi*

Urban Institute & School of Engineering, Kyushu University, Japan

ARTICLE INFO

Edited by Dr. Menghua Wang

Keywords:

Monthly ground-level NO₂ concentration
GWPR model
Spatial nonstationarity
OMI

ABSTRACT

Predicting long-term ground-level nitrogen dioxide (NO₂) is important globally to support environmental and public health research and to provide information to governments and society for air pollution control policies. The ozone monitoring instrument (OMI), onboard Aura Satellite, detects monthly global tropospheric column amounts (TrCA) of NO₂ molecules. However, the relationship between the ground-level NO₂ concentration and TrCA of NO₂ molecules remains elusive because NO₂ molecules in the air are not evenly distributed vertically. We use geographically weighted panel regression (GWPR) to examine the relationship between satellite-derived data, measured ground-level NO₂ concentrations, and several controlling meteorological variables from January 2015 to October 2021. The GWPR can analyze unbalanced panel data and capture the spatial variability of the relationship. Based on the GWPR estimation, 82 monthly global ground-level NO₂ concentrations are predicted from January 2015 to October 2021. The GWPR is reliable, as indicated by the 10-fold cross-validation. The accuracy of the raster prediction of global ground-level NO₂ from January 2015 to October 2021 is 69.61%. The coefficient of correlation, root mean square error and mean absolute error between globally predicted and measured ground-level NO₂ are 0.838, 7.84 $\mu\text{g}/\text{m}^3$ and 4.07 $\mu\text{g}/\text{m}^3$, respectively, while the mean of globally measured ground-level NO₂ is 19.47 $\mu\text{g}/\text{m}^3$. Overall, this research provides critical basic data to environmental and public health science and valuable information for governments and societies to make more reasonable policies.

1. Introduction

The air pollutant nitrogen dioxide (NO₂) is adversely related to various health outcomes (Lelieveld et al., 2015; Newell et al., 2017; Ogen, 2020; Orellano et al., 2020). The relationship between all-cause mortality and NO₂ concentration is positive (Brunekreef and Holgate, 2002). Specifically, a 10 $\mu\text{g}/\text{m}^3$ increase in NO₂ concentration in the short term is associated with a 0.72% increase in the relative risks of all-cause mortality (Orellano et al., 2020). The European Union and World Health Organization (WHO) recommend that the annual average exposure to ambient NO₂ should be lower than 40 $\mu\text{g}/\text{m}^3$. Additionally, other air pollutants, such as particulate matter and ozone, are associated with approximately 3.3 million premature deaths per year globally, and NO₂ is one of the critical ozone precursors (Beckerman et al., 2008; Lelieveld et al., 2015). Evidence shows a link between NO₂ and various acute and chronic diseases, especially decreased lung function and lung cancer (Chiusolo et al., 2011; Hamra et al., 2015; Rice et al., 2013). Furthermore, several studies, while controlling for several other crucial

factors, including age, gender, and restriction policy, indicate that in areas with high NO₂ concentrations, people are more easily infected by the coronavirus and find it more difficult to recover (Li and Managi, 2022; Ogen, 2020; Wu et al., 2020; Yao et al., 2021). In addition, air pollution affects human well-being directly (Li and Managi, 2021b). For example, an increase of 10 $\mu\text{g}/\text{m}^3$ in annual average NO₂ is related to an approximately 50% decrease in life satisfaction in London (Mackrill and Mourato, 2009). Thus, the ground-level NO₂ concentration affects human well-being and public health the most (Lelieveld et al., 2015; Li and Managi, 2021b, 2022). However, satellite measurements focus mainly on the tropospheric column amounts (TrCA) and the total column amounts (ToCA) of NO₂ (Fig. 1) (OMI Team, 2012). The association of the ground-level NO₂ concentration with TrCA and ToCA remains unclear because the NO₂ molecules are not vertically evenly distributed in the air. Several recent studies have investigated the regional ground-level NO₂ concentrations based on satellite observations. For example, Kim et al. estimated the hourly near-surface NO₂ in the alpine domain from June 2018 to May 2020 (Kim et al., 2021); Li et al. detected the

* Corresponding author at: Kyushu University, 744 Motooka, Nishi-ku, Fukuoka 819-0395, Japan.
E-mail address: managi@doc.kyushu-u.ac.jp (S. Managi).

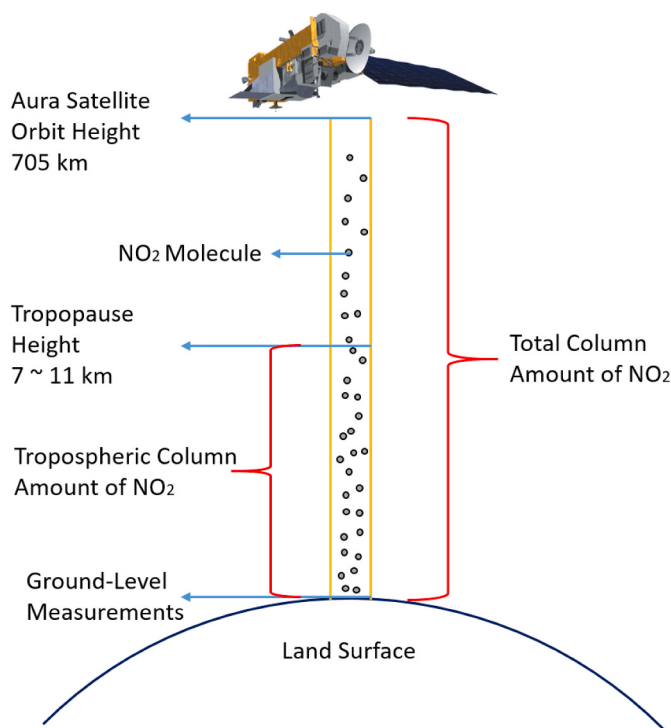


Fig. 1. Illustration of TrCA, ToCA, and ground-level measurements.

ground-level NO₂ concentrations in the Wuhan urban agglomeration during 2019 (Li and Wu, 2021; Li et al., 2020); and Qin et al. probed the ground-level NO₂ over central-eastern China from May 2013 to April 2014 (Qin et al., 2017). However, there is a lack of ground-level NO₂ concentration measurements in low-income countries, which induces broad uncertainty in the global ground-level NO₂ distribution (Larkin et al., 2017). However, to help detect the adverse impacts of NO₂ on public health and human well-being, global time-series ground-level NO₂ data are strongly desired.

Geographically weighted regression (GWR) is an advanced method that estimates air pollution while taking the spatial contexts into account (Bigdely et al., 2021; Jiang et al., 2017). To examine the relationship between satellite-derived data and measured ground-level air pollution, a variety of models have been developed, such as land-use regression (Bechle et al., 2015; Larkin et al., 2017), chemical transport models (Geddes et al., 2016), linear regression model (Lin et al., 2019; Liu et al., 2017), GIS-based multisource and multibox models (Wang and Chen, 2013), geographically and temporally weighted regression (GTWR) (Li et al., 2020; Qin et al., 2017), and machine learning methods (Kim et al., 2021). All these models show relatively high accuracy in the estimations. To further improve the accuracy, we take the spatial variability of the relationship between satellite-derived data and measured ground-level air pollution into account. The GWR can illustrate the spatial variability of the relationship according to the local regression technique and spatial weights (Fotheringham and Oshan, 2016; Hu et al., 2013). It must be noted that here, the global models are not spatially global models but statistically global models. The statistically global models mainly investigate the conditional interactions between the dependent and independent variables on the complete dataset, while the statistically local models are based on a partial dataset taking each observing subject as the center (Beenstock and Felsenstein, 2019).

Currently, GWR can only analyze cross-sectional data (data collected by observing many subjects at one period of time) or panel data (data collected by observing many subjects across time) by using pooled ordinary least squares (POLS). To incorporate the temporal effect into the analysis, there are two other advanced methods, namely, GTWR (Fotheringham et al., 2015; Qin et al., 2017) and geographically

weighted panel regression (GWPR) (Yu et al., 2021), to regress the balanced panel data (data collected by observing many subjects at all periods during the study period). GTWR is a spatially and temporally nonstationary model. Integrating spatial and temporal distance into spatiotemporal distance poses fresh unknowns, although Euclidean distance is still a powerful tool (Fotheringham et al., 2015; Li and Managi, 2021a; Qin et al., 2017). Furthermore, the recent GTWR model requires that the input dataset is a balanced panel dataset (Gollini et al., 2015). Yu et al.'s GWPR improves GWR by using the least squares dummy variable estimator, but models with other effects, such as fixed effects and random effects, are under development (Yu et al., 2021). This method works when the panel data have only a handful of periods. Moreover, neither of these two methods can solve the problem with unbalanced panel data (except balanced panel data, all panel data are unbalanced) due to the issues in the spatially weighted matrix. However, this limitation in the GWPR model is induced by the current toolboxes in most statistical software rather than the GWPR algorithm itself, although none of the current toolboxes specifically addresses the GWPR. For example, the outstanding GWR package "GWmodel" in R can also execute GWPR in specific situations using pretransformed datasets. However, this algorithm builds spatially weighted matrix rows for each observation, which consumes a large volume of computer memory and might cause failure due to a lack of memory. Furthermore, when it calibrates the adaptive distance bandwidth in GWPR using unbalanced panel data, it might miscalculate the numbers of spatial neighbors of some observations because the observation numbers vary in each location in unbalanced panel data. In fact, most observed datasets are unbalanced, including our dataset. To analyze the panel data by GWPR and facilitate other researchers, we bundle the GWPR algorithm into a new R package, "GWPR.light" (<https://cran.r-project.org/web/packages/GWPR.light/index.html>), and release it on CRAN (The Comprehensive R Archive Network). The "GWPR.light" requires less memory even for big data calculations, solves the issues of the numbers of spatial neighbors of observations, and can perform GWPR with fixed or random effects.

In this paper, first, based on a series of statistical tests and model comparisons, we choose the GWPR with fixed time-fixed effects. This GWPR model has excellent accuracy. Second, the GWPR analysis involves several auxiliary variables, including terrain atmospheric pressure, land surface temperature, normalized difference vegetation index (NDVI), precipitation, planetary boundary layer height (PBLH), and year dummy variables, to detect the relationship between the ground-level and TrCA of NO₂. Third, we calibrate the optimal bandwidth, which is critical to building the spatially weighted matrix. Fourth, we estimate the spatially nonstationary coefficients using the GWPR model, then interpolate the coefficients into raster data. Finally, we provide the monthly global ground-level NO₂ concentration from January 2015 to October 2021.

2. Materials and methodology

2.1. Materials

2.1.1. Satellite-derived NO₂ estimation

The satellite Ozone Monitoring Instrument (OMI) provides vertical column amounts of NO₂. The OMI/Aura NO₂ Total and Tropospheric Column Daily L2 Global Gridded 0.25 degree × 0.25 degree V3 (OMNO2G) is the global daily grid dataset with a 0.25-degree resolution to gauge TrCA and ToCA of NO₂ (Fig. 1). It is based on the observation of the NASA Earth Observing System (EOS) Aura satellite platform (Irie et al., 2012; Li and Wu, 2021; Nickolay et al., 2019) (https://disc.gsfc.nasa.gov/datasets/OMNO2G_003/summary). This satellite was launched on July 15, 2004, and began providing daily global TrCA, stratospheric column amounts and ToCA of NO₂ observations (unit: molecules/cm²) from October 1, 2004 (Nickolay et al., 2019; OMI Team, 2012). The OMI-NO₂ datasets, especially OMNO2G, have been widely used in emission and pollution monitoring (Curier et al., 2014; Li and

Wu, 2021; Liu et al., 2017). Air pollution near the surface impacts human health and daily life most harmfully (Hamra et al., 2015; Rice et al., 2013). However, the ground-level NO₂ concentration is unavailable in many areas, particularly in rural areas and most developing countries. Therefore, the conversion or estimation from TrCA or ToCA to ground-level data becomes a critical issue. The EOS Aura orbit is a sun-synchronous polar orbit at an altitude of 705 km, and the satellite goes over each location between 12:00 and 15:00 local time (OMI Team, 2012; Schoeberl et al., 2006). Due to the orbit altitude, the ToCA of NO₂ covers the NO₂ molecules in the troposphere, stratosphere, mesosphere, and thermosphere, while the TrCA of NO₂ takes only the troposphere into account. Because the troposphere is most affected by human activities and air pollution, it has the most substantial impact on human health (Lelieveld et al., 2015; Li and Managi, 2022) and well-being (Li and Managi, 2021b), and the TrCA of NO₂ is an ideal independent variable to predict the ground-level NO₂ concentration. However, owing to anthropogenic climate change, tropopause height is slowly rising (Meng et al., 2021). Although this continuous rise is relatively small in comparison to the tropopause height, whether it influences the estimation of the TrCA of NO₂ remains elusive. To choose the satellite NO₂ variable, we put both the ToCA and TrCA of NO₂ in the analyses as the primary variables. Both the goodness of fit of the model taking the TrCA of NO₂ as the dependent variable (R^2 : 74.45%) and the cross validation results are slightly better than those of the other model using the ToCA of NO₂ (R^2 : 74.39%). Moreover, compared with the satellite orbit height, the tropopause height is closer to the surface, which might make the TrCA of NO₂ more accurate. Therefore, the TrCA of NO₂ is employed in the final analysis.

We convert the unit of the TrCA of NO₂ from $molecules/cm^2$ to micrograms per square meter ($\mu g/m^2$), to make it understandable to the public as follows:

$$ATrCA = RTrCA / N_A \times MM_{NO_2} \times 10,000 cm^2 / m^2 \times 1,000,000 \mu g/g \quad (1)$$

where $ATrCA$ is the TrCA of NO₂ after the unit conversion, whose unit is $\mu g/m^2$, $RTrCA$ is the value extracted from the OMNO2G directly, whose unit is $molecules/cm^2$, N_A is the Avogadro constant ($6.022 \cdot 10^{23} mol^{-1}$), and MM_{NO_2} is the molar mass of NO₂ (46.007 g/mol).

The temporal resolution of our analysis is monthly, although both the OMNO2G and ground-level measurements are seemingly daily. Due to the orbit height of the EOS Aura, the satellite revisit period is 16 days and the orbit period is 98.83 min (Schoeberl et al., 2006). The EOS Aura's telescope field of view is 2600 km on the ground. Its daily data are from the day-lit portion of the satellite's 14 orbits. For all these reasons, each location could be observed several times in a month rather than every day. In other words, some locations are unobserved in a few days. Furthermore, other auxiliary satellite data, such as land surface temperature and NDVI, are obtained from the EOS Terra and Aqua satellites, whose satellite revisit periods are also 16 days. For these reasons, we convert the daily TrCA of NO₂ from the OMNO2G dataset into the monthly average TrCA of NO₂.

2.1.2. Ground-level NO₂ measurements

This dataset can be downloaded from the Air Quality Open Data Platform (<https://aqicn.org/data-platform/covid19/>). The data have been available in over 530 major cities since 2015. The data provider has converted to the unified unit, part per billion (PPB), in accordance with the requirement of the United States Environmental Protection Agency. Initially, the dataset included 539 cities, but nine were dropped because there were no more than five monthly records from January 2015 to October 2021. This study exploits the monthly average NO₂ concentration as the dependent variable, calculated from the daily data, to merge with the satellite data correctly. The Air Quality Open Data Platform also provides the locations of the cities with measurement points (<https://aqicn.org/data-platform/covid19/airquality-covid19-cities.json>) (Fig. 2, Supplementary Materials Table S1: City List). In

most cities, there are generally several measurement points. The dataset records the medians of ground-level NO₂ using the data from different measurement points in a specific city. The ground-level measured NO₂ concentration data are daily data. To connect them with the satellite data, we convert them into monthly average values. It must be underscored that we use all the daily observations to calculate the monthly mean of ground-level NO₂. However, there is no significant difference between the means obtained from all the daily observations and using the observations sampled at OMI measurement dates. In particular, the correlation between the means in each measurement using all the daily observations and using the observations sampled at OMI measurement dates is 0.980 (p value <0.1%). The variation caused by the difference is only 4.17% of the total variation of the means using all daily observations. Therefore, the means of all the daily observations are valid. Additionally, OMNO2 is a Level-2 grid product. The missing values of the satellite measurement appear in the data swath gaps. Even though the satellite does not observe a specific city on a certain day, other grids close to that city might be detected. Thus, ignoring some ground-level measurements due to no satellite data might decrease the accuracy of predictions.

The unit of monthly average ground-level measured NO₂ concentration data is PPB, while the unit of the monthly average TrCA of NO₂ is micrograms per square meter ($\mu g/m^2$). To make the units of these two datasets consistent, we convert the unit of monthly average ground-level measured NO₂ concentration data from PPB to $\mu g/m^3$ using the following equation:

$$GNO_2 = \frac{P \times MW_{NO_2} \times RGNO_2}{R \times T \times 1000} \quad (2)$$

where GNO_2 is the monthly average ground-level NO₂ concentration with unit $\mu g/m^3$, $RGNO_2$ is the NO₂ concentration before conversion, whose unit is PPB, P is the terrain atmospheric pressure (mmHg), which can be extracted from OMNO2G and converted into the monthly average values (OMNO2G data unit is hPa, and the conversion coefficient between mmHg and hPa is 0.750 mmHg/hPa), MW_{NO_2} is 46.007, R is the ideal gas constant ($62.4 L \bullet Torr \bullet K^{-1} \bullet mol^{-1}$), and T is the monthly average temperature from MODIS product, MOD11C3.

2.1.3. Auxiliary data

Auxiliary data, including terrain atmospheric pressure, temperature, NDVI, precipitation, and PBLH, are taken as the control variables to improve the model's performance. A considerable number of previous studies have involved terrain atmospheric pressure in the analyses of NO₂ concentrations (Chi et al., 2021; Li et al., 2020). Terrain atmospheric pressure data are from OMNO2G, with a 0.25-arc-degree resolution. Although the temporal resolution of this dataset is daily, it has the same problem as the TrCA of the NO₂ dataset, namely, a long satellite revisit period of the Aura satellite. Therefore, we convert it into a monthly average value. Additionally, to make the calculation understandable, the unit of land surface temperature is converted into Celsius.

The temperature data are provided by the Moderate Resolution Imaging Spectroradiometer (MODIS, <https://modis.gsfc.nasa.gov/>). The products, MOD11C3 and MYD11C3, are based on the MODIS Terra and Aqua satellite observations and measurements, including the daytime and nighttime average temperatures, with a 0.05-arc-degree spatial resolution (<https://modis.gsfc.nasa.gov/data/dataproduct/mod11.php>). Due to the 16-day revisit period, there are one or two global raster data based on each satellite's monthly observation. In a month, we take the mean of all the raster data, involving the daytime and nighttime average temperature in a month, to obtain the monthly average temperature raster. We note that the spatial resolution of the monthly average temperature raster is still 0.05 arc degrees. To make it consistent with the monthly average TrCA of NO₂, we reduce the resolution to 0.25 arc degrees by applying the average value.

The monthly NDVI data are acquired from the MODIS products,

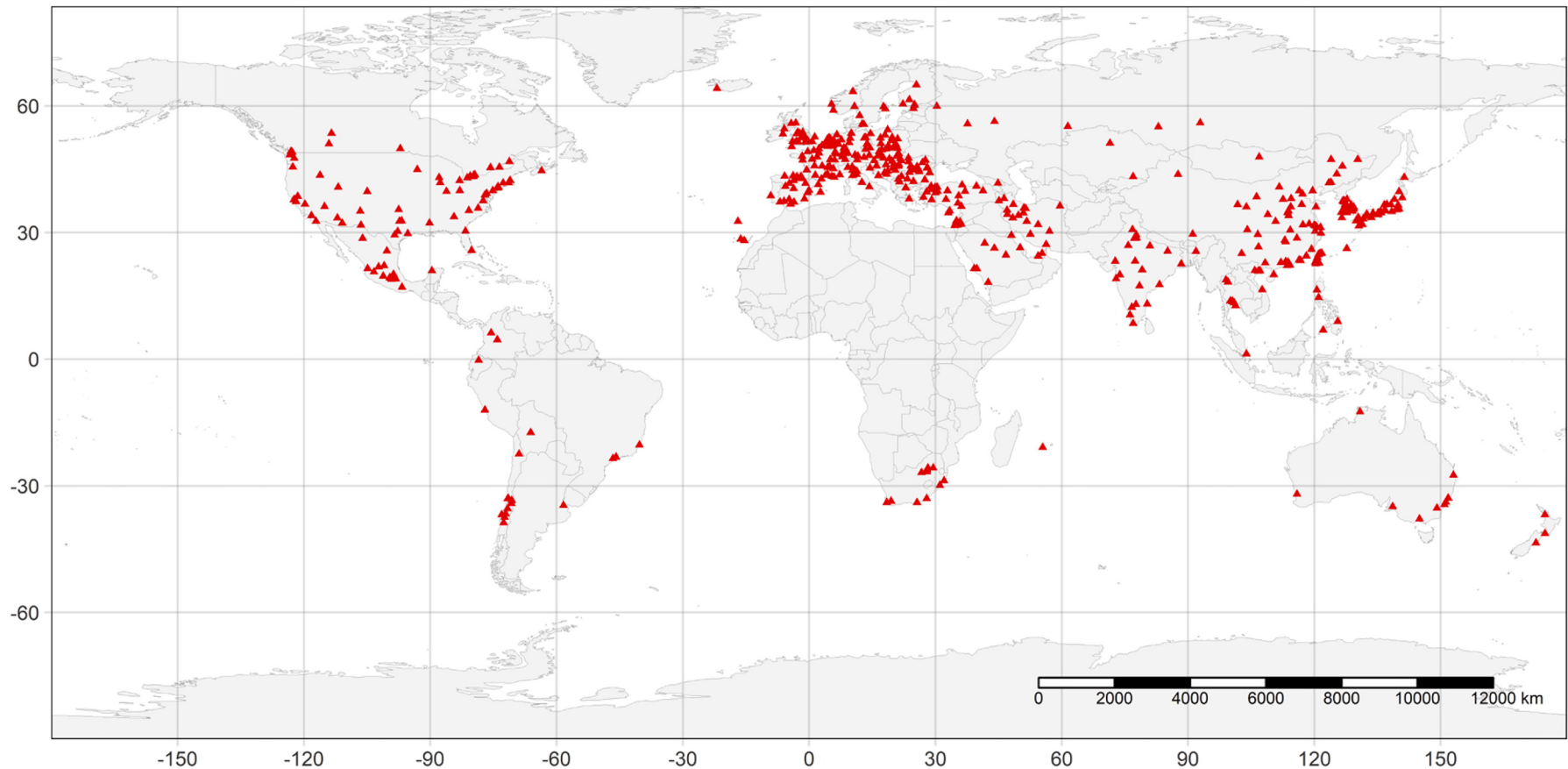


Fig. 2. Map of city locations with the measurement points.

MOD13C2 and MYD13C2 (<https://modis.gsfc.nasa.gov/data/dataprod/mod13.php>), with a 0.05-arc-degree spatial resolution. We also use the average value to make its resolution 0.25 arc degrees. The NDVI value ranges from -1 to 1. Because the ground-level NO₂ data are from cities, the situation in rural areas is not carefully gauged. To enable the model to predict the environment in rural areas, we incorporate the NDVI into the analysis since the most notable difference between urban and rural areas is landscape and human activity density. Both the NDVI and land cover raster can depict landscape, but land cover data are discrete and yearly and hence are not applicable for this analysis. Therefore, we employ the NDVI to reduce the influence of the difference between

urban and rural areas. Additionally, nighttime light is associated with transportation (Chang et al., 2019) and human activity (Zhao et al., 2019), which are related to air pollution emissions. To represent their impacts, we also put the nighttime light data into the initial model. However, this has little effect on the prediction accuracy. Hence, it is removed in the final model.

The precipitation data are obtained from NASA Global Land Data Assimilation System Version 2 (GLDAS) Noah Land Surface Model L4 monthly $0.25 \times 0.25^\circ$ V2.1 (GLDAS_NOAH025_M, https://disc.gsfc.nasa.gov/datasets/GLDAS_NOAH025_M_2.1/summary). The temporal and spatial resolutions are one month and 0.25 arc degrees, respectively.

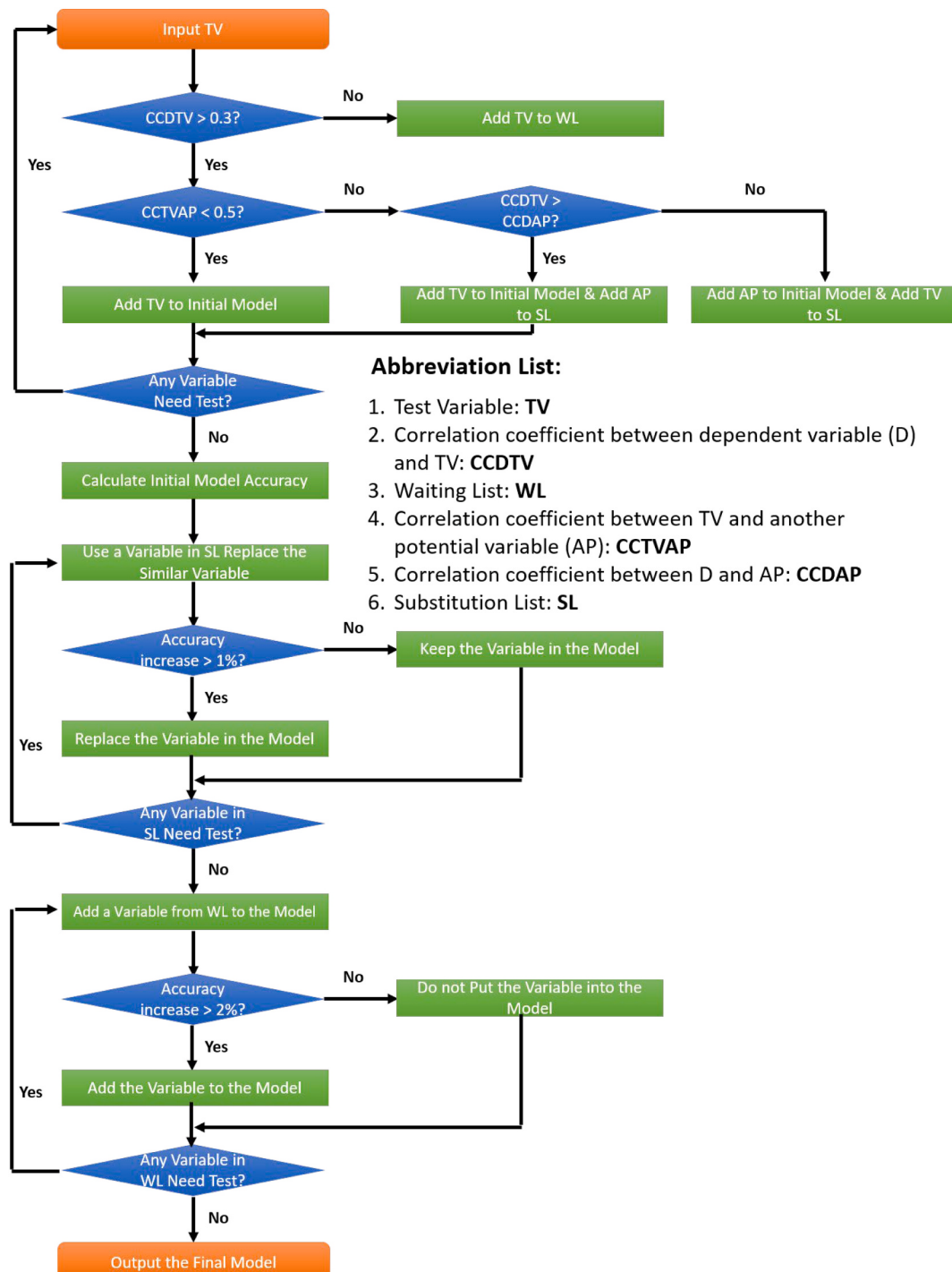


Fig. 3. Flow chart of variable selection process.

This dataset has some missing values because some regions are too close to the seas and oceans. To avoid the reduction of the data size in our calculation, we impute the missing values by averaging their closest surrounding grids. We estimate the dataset twice, that is, the original GLDAS_NOAH025_M dataset boundary extends approximately 0.5 arc degrees into the seas and oceans. The original unit of this dataset is $\text{kg}/(\text{m}^2 \cdot \text{s})$, but most values are $<0.0001 \text{ kg}/(\text{m}^2 \cdot \text{s})$. To improve the readability and robustness of the calculation, we convert its unit to $\text{kg}/(\text{m}^2 \cdot \text{h})$.

The PBLH data are extracted from Monthly mean, Time-Averaged, Single-Level, Assimilation, Surface Flux Diagnostics V5.12.4 (M2TMNXFLX, <https://disc.gsfc.nasa.gov/datasets/M2TMNXFLX.5.12.4/summary>). The spatial resolution of this dataset is $0.5^\circ \times 0.625^\circ$. We employ the bilinear interpolation method to impute a new dataset with a 0.25-arc-degree resolution. The unit of PBLH is meters (m).

Fig. 3 demonstrates the variable selection process of this research. Simply put, we select a variable that meets one of the following three requirements. First, the variable is significantly related to the dependent

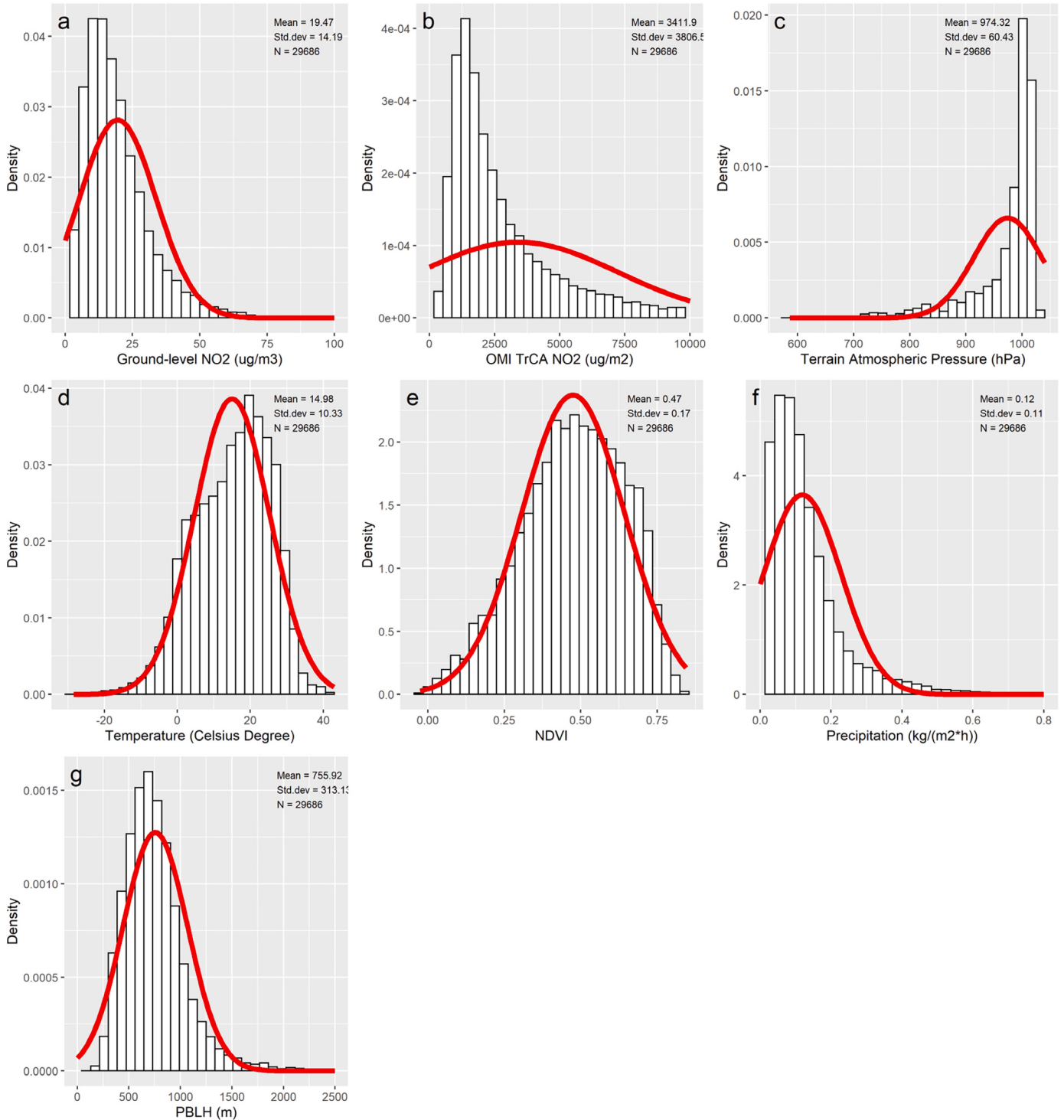


Fig. 4. Statistical distributions and descriptive statistics of the variables in the original dataset.
(The red line is the normal curve.)

variable and has low correlations with other variables in the model. Second, the variable can significantly improve the model accuracy. Third, previous studies prove that the variable is necessary for the analysis. In the model design stage, we consider many other variables, including humidity, nighttime light, wind speed, cloud pressure, aerosol optical depth, and ultraviolet aerosol index. However, none of these variables are effective due to either their poor contribution to improving the prediction accuracy or due to the multicollinearity between independent variables. For example, the correlation coefficient between

humidity and precipitation significantly exceeds 0.5. Furthermore, the correlation coefficient between humidity and temperature is over 0.7, while the relationship between precipitation and temperature is not as strong, namely, 0.15. Therefore, we keep the precipitation and temperature in the analysis. Moreover, the GWPR results are spatial point data frames. To secure the coefficient raster data for the prediction, we have to employ interpolation methods, which would cause some slight errors. If the benefit of involving one more variable cannot offset the errors in its interpolation, it should not be taken into account. In view of

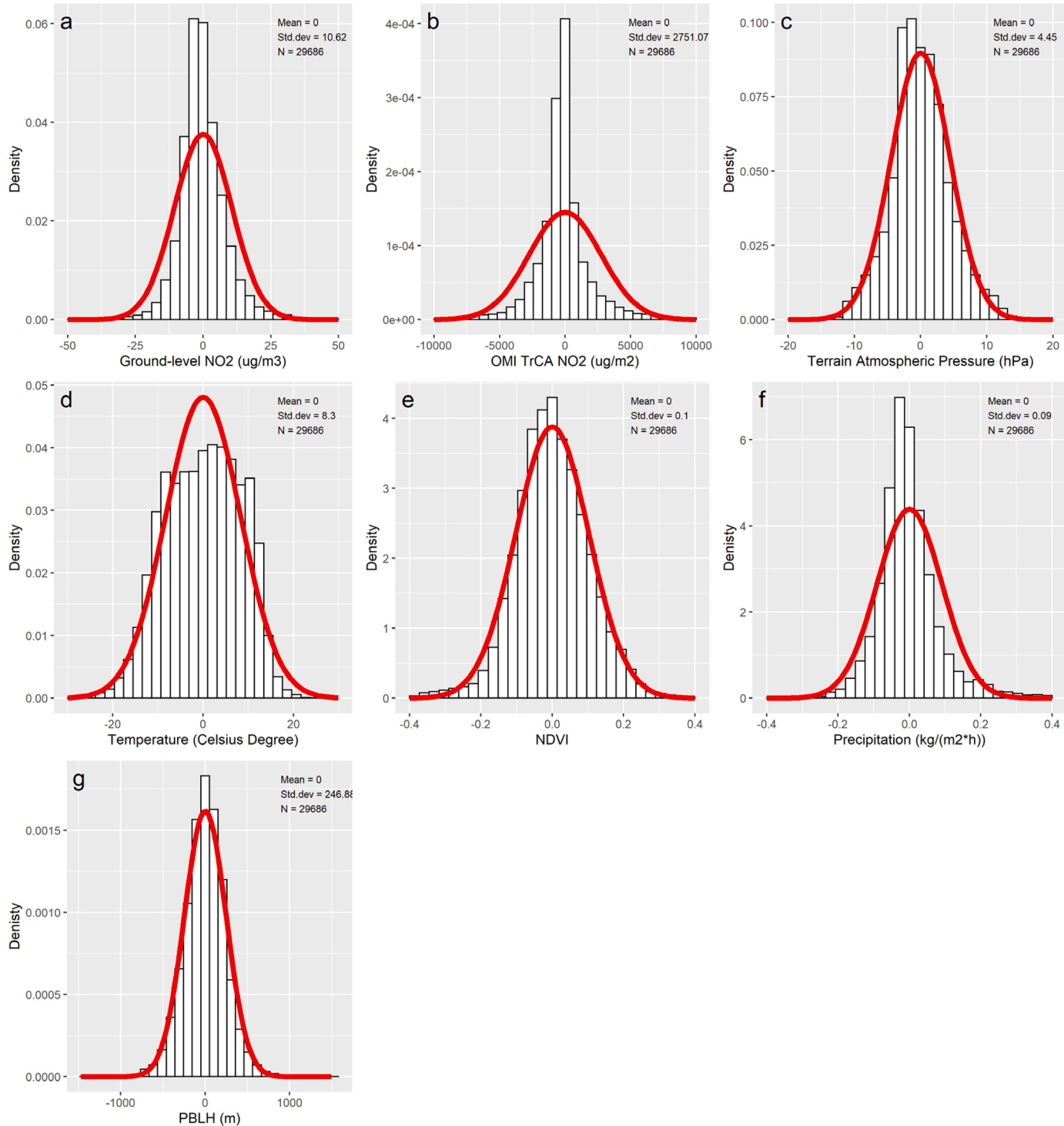


Fig. 5. Statistical distributions and descriptive statistics of the variables in the transformed dataset.
(The red line is the normal curve.)

numerous tests, finally, we select the TrCA of NO₂, terrain atmospheric pressure, temperature, NDVI, precipitation, and PBLH as independent variables.

2.1.4. Descriptive statistics

We establish an unbalanced dataset based on the above data sources for modeling and prediction with timestamps and geographical locations from January 2015 to October 2021. The number of complete observations in this dataset is 29,686. The imbalance of data is expressed in both temporal and spatial extent. Every city has at least five months and at most 65 months of data, i.e., it is the imbalance in temporal extent. Moreover, the spatial distribution is also unbalanced. For instance, the smallest distance between the two closest cities is 0.103 arc degrees, while the largest distance is 24.710 arc degrees. As shown in Fig. 2, most cities with the data are located in the Northern Hemisphere, while only a few are distributed in South America, Africa, and Australia, which increases the difficulty of the interpolation.

Fig. 4 summarizes the statistical distributions and descriptive statistics of the variables in the original dataset. The statistical distribution of the concentration of ground-level NO₂ is one peak and right-skewed because the skewness is 7.17. Due to the 4.17 skewness, the statistical distribution of the monthly TrCA of NO₂ is one right-skewed peak. The statistical distribution of terrain atmospheric pressure is one left-skewed peak, whose skewness is -2.37. The shape of the monthly average temperature distribution is one slightly left-skewed peak because its skewness is -0.39. The statistical distribution of NDVI is one peak and slightly left-skewed (skewness: -0.34). The shape of its statistical distribution of precipitation is one right-skewed peak because its skewness

is 2.25. The statistical distribution of the PBLH is one right-skewed peak (skewness: 1.79). According to the variable distribution shape illustrated in Fig. 4, some variable distributions cannot be deemed normal distributions. Therefore, directly putting them into regression is unsuitable. Put another way, the POLS cannot be employed as the basic analysis model.

We choose instead the fixed effect model (FEM) as the basic algorithm based on a series of statistical tests. This will be described in the next section. In FEM, the data are transformed as follows:

$$\tilde{V}_{it} = V_{it} - \bar{V}_i \quad (3)$$

where \tilde{V}_{it} denotes the transformed dependent and independent variables in measurement i during month t , V_{it} denotes the original dependent and independent variables in measurement i during month t , and \bar{V}_i denotes the mean values of each original variable in measurement i . Fig. 5 demonstrates the variable distributions in the transformed dataset. The variables in the transformed dataset are almost normally distributed because their skewnesses and kurtoses are close to 0 except for ground-level NO₂, monthly TrCA of NO₂, and precipitation. The distributions of those three variables in the transformed dataset are right-skewed and leptokurtic because their skewnesses are 11.74, 4.00, and 1.68, and their kurtoses are 556.92, 54.23, and 10.11, respectively. We find that the transformed dataset still has 17 extremely large numbers of ground-level NO₂, which are more than ten standard deviations from the mean. They mainly appear in five cities, including Izmir (Turkey), Konya (Turkey), Khorramabad (Iran), Qom (Iran), and Puebla (Mexico). If we ignore these extreme numbers, the skewness and kurtosis decrease

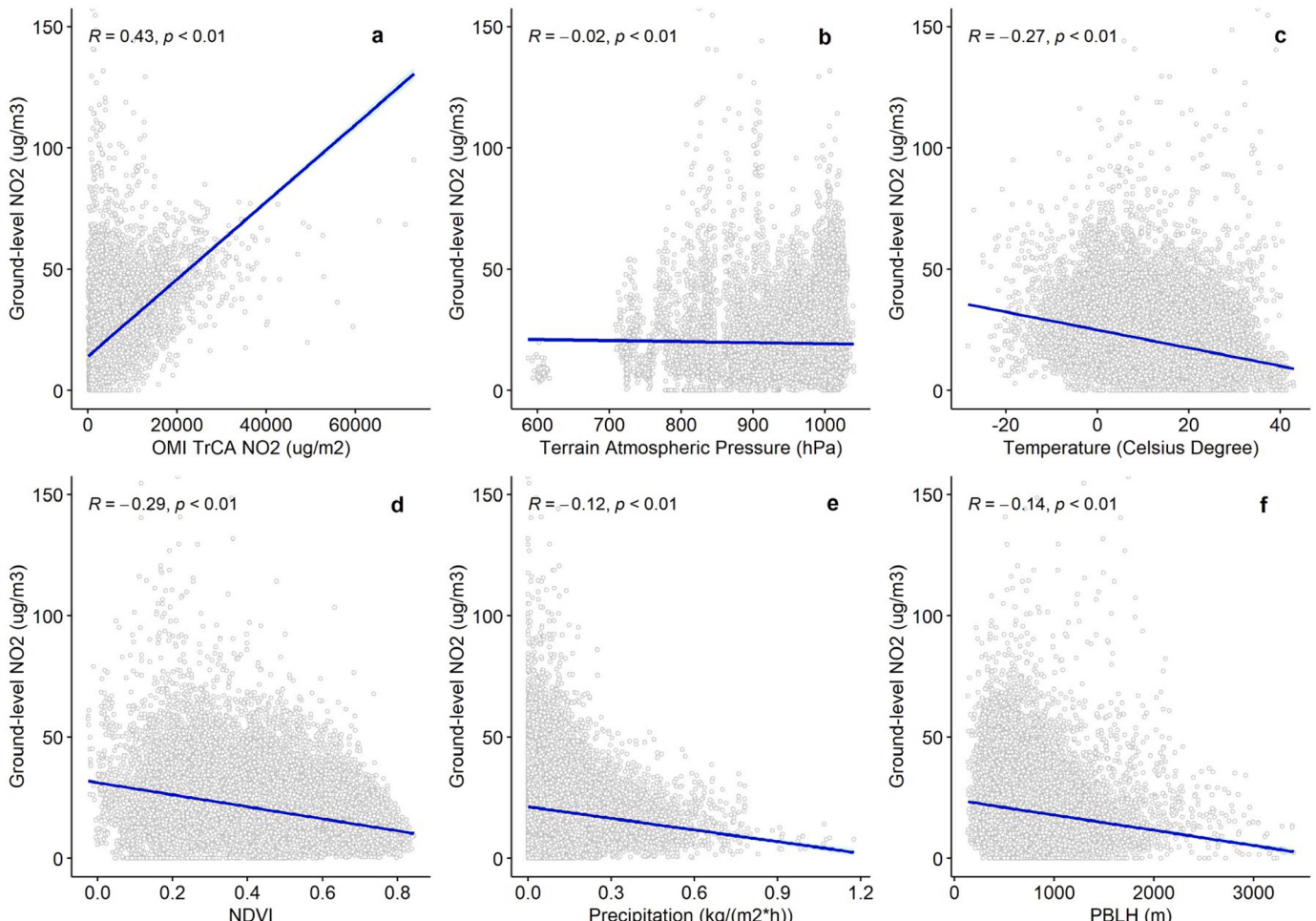


Fig. 6. Linear trends and correlation coefficients between variables in the original dataset.

significantly. It must be underscored that the extreme numbers in the transformed dataset mean that the variable in specific measurements fluctuated significantly, rather than that they are absolutely large. The variables, monthly TrCA of NO₂ and precipitation, show similar situations, although extreme values appear in different cities. Because the share of the extreme numbers is no >0.5%, their impacts on regression can be ignored.

Figs. 6 and 7 show the linear trends and correlation coefficients between the concentration of ground-level NO₂ and other variables in the original and transformed datasets, respectively. In Figs. 6 and 7, r and p represent Pearson's correlation coefficient and p value, respectively (Taylor, 1990). r is calculated as follows:

$$r = \frac{\sum_{i=1}^n (X1_i - \bar{X1})(X2_i - \bar{X2})}{\sqrt{\sum_{i=1}^n (X1_i - \bar{X1})^2} \sqrt{\sum_{i=1}^n (X2_i - \bar{X2})^2}} \quad (4)$$

where r is the correlation coefficient, $X1$ and $X2$ are the aimed variables put into the test, and n is the data size. To estimate the significance of the correlation coefficient, we calculate the t -test value (t) at first:

$$t = \frac{r\sqrt{n-2}}{\sqrt{1-r^2}} \quad (5)$$

Here, the p value (p) is calculated as follows:

$$p = 2 \times \Pr(T > t) \quad (6)$$

where T follows a t distribution with $n - 2$ degrees of freedom, and $\Pr(T >$

$> t)$ represents the probability of $T > t$. According to Figs. 6 and 7, all correlation coefficients are significant at the 0.1% level.

2.2. Methodology

2.2.1. Spatially stationary global model

We first assume that the relationships between the ground-level concentration of NO₂ and other independent variables are spatially stationary (Brunsdon et al., 1998; Fotheringham et al., 2002). We apply the three typical global models, namely, the random effects model (REM), FEM, and POLS, to estimate the relationships among the variables. The only difference between these three global models is the time-fixed effects in the models. Therefore, substantial tests about the time-fixed effects are needed.

We select global models with different time-fixed effects, namely, REM, FEM, and POLS. To compare FEM with POLS, we apply the F test for individual effects. FEM is better than POLS since the test result is significant, and the null hypothesis that no time-fixed effects are needed is rejected (Breusch and Pagan, 1980; Croissant and Millo, 2008). Based on the Breusch-Pagan Lagrange Multiplier test for random effects, the significant result indicates that REM is appropriate because the null hypothesis that no time-fixed effects are needed is not accepted (Breusch and Pagan, 1980). We also run the Hausman test to detect a reasonable model between FEM and REM (Kang, 1985). The significant result indicates that FEM is preferred, as the null hypothesis that the preferred model is REM is rejected. Here, the FEM in our analysis is as follows:

$$GNO2_u = \beta X'_{it} + \alpha_i + \mu_{it} \quad (7)$$

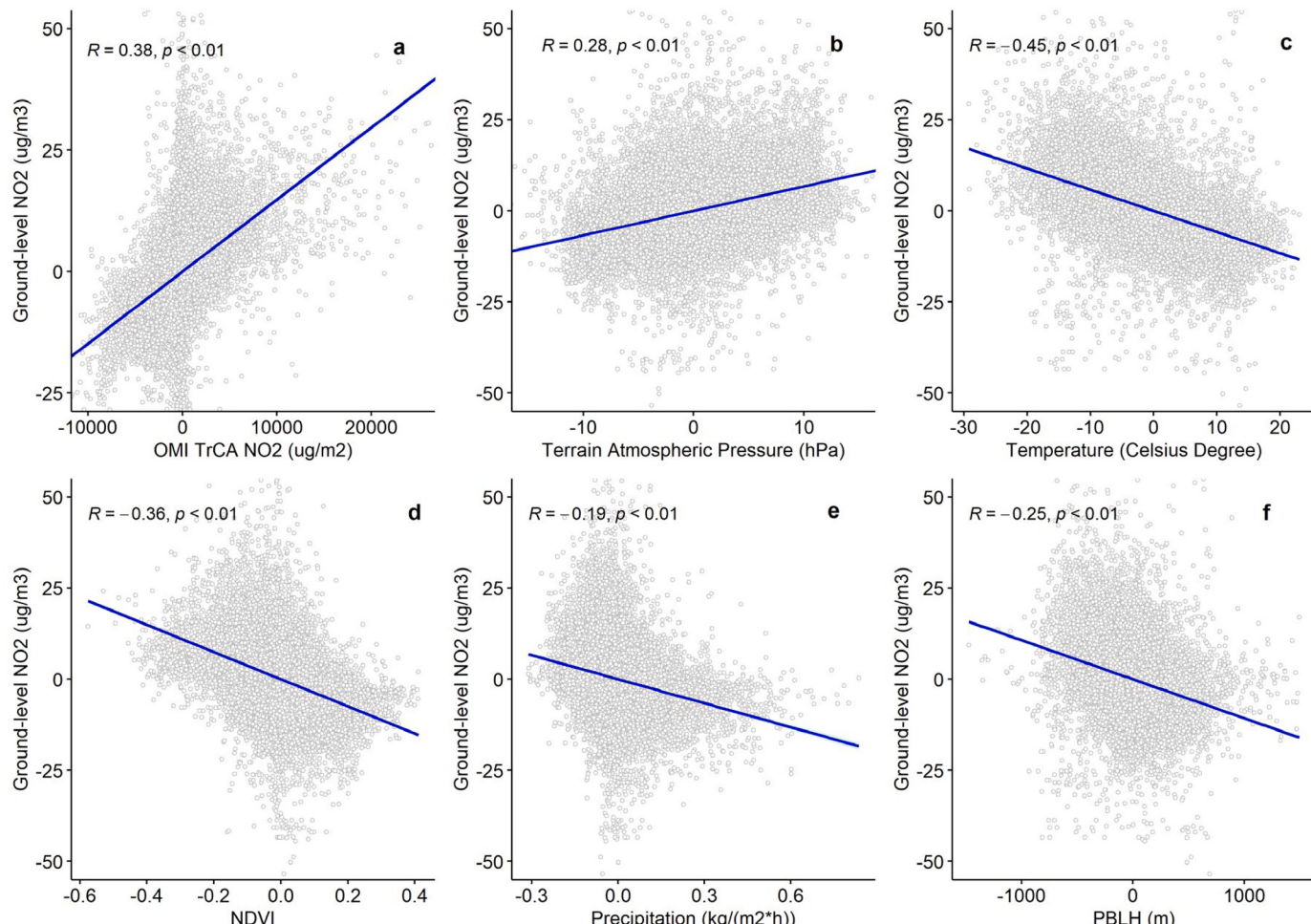


Fig. 7. Linear trends and correlation coefficients between variables in the transformed dataset.

where $GNO2_{it}$ denotes the monthly average ground-level concentration of NO_2 ($\mu\text{g}/\text{m}^3$) in measurement i during month t , \mathbf{X}_{it} denotes a matrix of independent variables, including TrCA of NO_2 ($\mu\text{g}/\text{m}^2$), terrain atmospheric pressure (hPa), temperature ($^\circ\text{C}$), NDVI, precipitation ($\text{kg}/(\text{m}^2 \cdot h)$), PBLH (m), and year dummy variables in measurement i during month t , α_i denotes the time-fixed effects, μ_{it} denotes an idiosyncratic error, and β is a vector of parameters to be estimated. Some ignored variables, such as air pollution policy in countries and economic status, among others, are changed year by year. We therefore add the year dummy variables to the model.

2.2.2. Spatially nonstationary local model

Unlike global linear regression models, including REM, FEM, and POLS, the GWPR allows the coefficients to vary spatially (Brunsdon et al., 2010; Fotheringham and Oshan, 2016). Because the relationship between the dependent variable and the independent variables could vary by the spatial context, the estimation accuracy of the ground-level NO_2 concentration, such as the goodness of fit of the models, dramatically improves. Basically, the GWPR divides the total sample into numerous subsamples according to the optimal bandwidth and spatially weighted matrix. The bandwidth in GWPR is the threshold distance to judge whether two objects have a spatial relationship (Beenstock and Felsenstein, 2019; Brunsdon et al., 2010; Brunsdon et al., 1998). If two objects have a spatial relationship, they are considered to be neighbors of each other. Currently, two types of bandwidth are widely used, fixed distance bandwidth and adaptive distance bandwidth (Gollini et al., 2015). The fixed distance bandwidth is a fixed threshold distance, and if two spatial objects are within this distance, they are spatially related. The adaptive distance bandwidth is the number of objects in a subsample because every object always has a certain number of neighbors. Hence, the threshold distance for each object might be different. To calibrate the optimal bandwidth in the GWPR, the mean square prediction error is the critical index. When the mean square prediction error is the smallest, the model with a certain bandwidth has the highest accuracy (Gollini et al., 2015). For a specific bandwidth (b), the mean square prediction error is calculated as follows:

$$MSPE(b) = \frac{m \sum_j [y_j - \widehat{y}_j(b)]^2}{(m - p + 1)^2} \quad (8)$$

where $MSPE(b)$ is the mean square prediction error based on a specific bandwidth b , m is the data size, y_j is the dependent variable's value of the j th record, $\widehat{y}_j(b)$ is the predicted value of the j th record based on bandwidth b , and p is the number of parameters in the analysis. It must be

noted that bandwidth b can be either the fixed distance bandwidth or the adaptive distance bandwidth here. The GWPR is an improvement of GWR in that it considers time-fixed effects. In GWR, previous studies generally assume that Eq. 8 is a U-shaped function (Brunsdon et al., 1998; Fotheringham et al., 2002; Gollini et al., 2015). However, as those studies mentioned, there is no statistical or mathematical evidence for or against this assumption. The benefit from this assumption is the reduction of calculating time because the calculation could use the golden-section search to find the extremum to obtain optimal bandwidth (Gollini et al., 2015).

The step increment selection is applied to calibrate the optimal bandwidth due to the recently designed program that requires fewer computer resources. We calibrate the optimal fixed and adaptive distance bandwidths. In the fixed distance bandwidth selection, the selection extent is from 0.25 arc degrees to 20 arc degrees, and the examined bandwidth increases by 0.25 arc degrees every time because the spatial resolution of all the grid data is 0.25 arc degrees. The optimal fixed distance bandwidth is 2.25 arc degrees (Fig. 8). Since the spatial distribution of the cities with data is unbalanced and some points are far from others (Fig. 2), many points would have no neighbor if using this bandwidth. Data islands severely destroy the stability of the GWPR because they have no relationship with other points in the dataset. Dropping the data islands and increasing the bandwidth would slash the accuracy of the analysis. Hence, we adopt the adaptive distance bandwidth. In the adaptive distance bandwidth selection, the selection extent is from 4 to 100, and the tested bandwidth increases by one every time. When the adaptive distance bandwidth is <4 , some local regressions do not have enough degrees of freedom. According to the analysis, the optimal adaptive distance bandwidth is selected, which is 7. In other words, in each subsample, every locally weighted regression involves seven cities' data.

The spatially weighted matrix, based on the calibrated bandwidth, is calculated as follows:

$$\mathbf{W}_i = \begin{cases} \left[1 - \left(\frac{\mathbf{d}}{b_i} \right)^2 \right]^2, & d_k \in \mathbf{d} \text{ if } d_k \leq b_i \\ 0, & d_k \notin \mathbf{d} \text{ if } d_k > b_i \end{cases} \quad (9)$$

where \mathbf{W}_i denotes a vector of spatial weights between city i and its neighbors, \mathbf{d} represents a vector of distances between city i and its neighbors, b_i is the threshold distance of city i 's neighbors, and d_k is the distance between city i and city k . It should be emphasized that b_i might vary city by city, as here we use the adaptive distance bandwidth. Every vector is a column of the spatially weighted matrix. According to the spatial weight vectors, the total sample is divided into 530 subsamples,

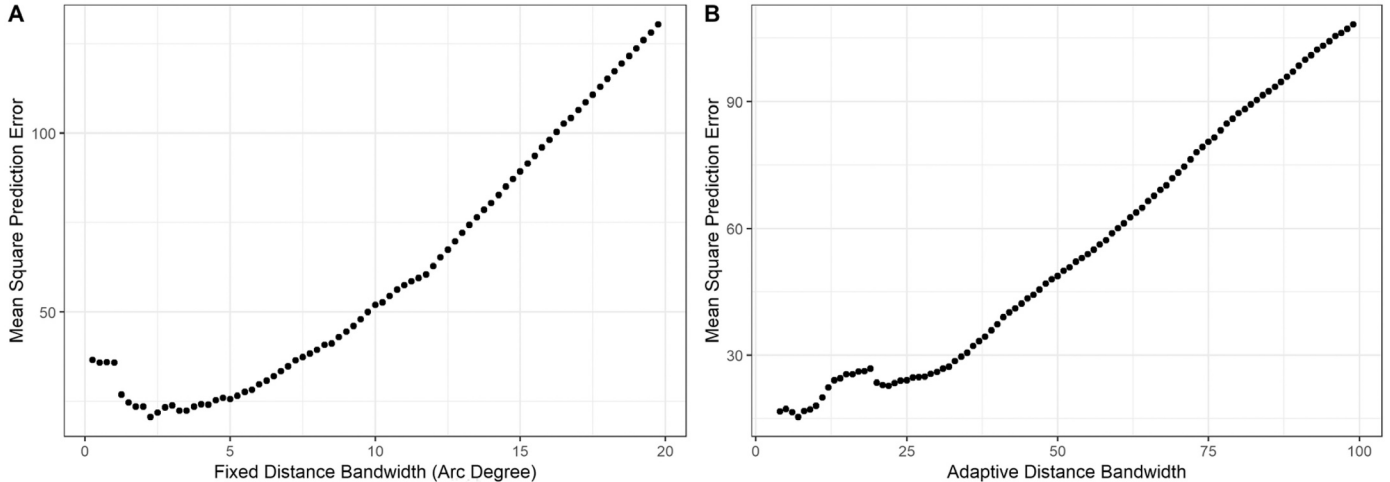


Fig. 8. Step increment bandwidth selection.

taking every city as the center.

The GWPR estimates the coefficients in every location in light of the spatially weighted matrix. In global model statistical tests, FEM is the preferred model, and in the locally statistical test, most local regressions show significant time-fixed effects. Therefore, the GWPR model also follows the FEM. The GWPR model is expressed as follows:

$$GNO2_{it} = \beta_i X'_{it} + \alpha_i + \epsilon_{it} \quad (10)$$

where β_i denotes a vector of parameters in the regression with the subsample taking city i as the center. In terms of the equation expression, the only difference between FEM (Eq. 7) and the GWPR based on FEM (Eq. 10) is that β_i varies spatially. It must be noted that the algorithm would change to the GWPR based on POLS if we directly used the GWR method. According to cross validation, the accuracy and stability of the GWPR based on POLS are lower than those of the GWPR based on FEM. Thus, the new method, GWPR, is necessary for this analysis.

To estimate the coefficient in the GWPR, because the time-fixed effects (α_i) are unknown (Croissant and Millo, 2008), we need to expand Eq. 10 as follows:

$$GNO2_{it} - \hat{\theta}_i \overline{GNO2_i} = (1 - \hat{\theta}_i) \beta_{0i} + \beta_i (X_{it} - \hat{\theta}_i \bar{X}_i)' + (\epsilon_{it} - \hat{\theta}_i \bar{\epsilon}_i) \quad (11)$$

where $\hat{\theta}_i$ denotes the share of the individual effects in the total effects, $\overline{GNO2_i}$ denotes the mean of the ground-level NO₂ concentration in the dataset in city i , β_{0i} is the estimated intercept in city i , \bar{X}_i denotes a vector of means of independent variables in city i , and $\bar{\epsilon}_i$ denotes the mean of the error in city i . If the GWPR follows the data transformation of FEM, $\hat{\theta}_i$ is always equal to 1. Therefore, β_{0i} is removed, in the GWPR based on FEM. To simplify Eq. 11, we define the matrix of independent variables x_{it} and the dependent variable $gno2_{it}$ as follows:

$$x_{it} = X_{it} - \bar{X}_i \quad (12)$$

$$gno2_{it} = GNO2_{it} - \overline{GNO2_i} \quad (13)$$

$$\sigma_{it} = \epsilon_{it} - \bar{\epsilon}_i \quad (14)$$

In light of Eqs. 12–14, the GWPR model is transformed as follows:

$$gno2_{it} = \beta_i x'_{it} + \sigma_{it} \quad (15)$$

This algorithm becomes the typical GWR without the intercept. The coefficient estimation can be displayed as follows:

$$\beta_i = [x_{it}^T W x_{it}]^{-1} x_{it}^T W_i gno2_{it} \quad (16)$$

2.2.3. Statistical indicators

Previous studies widely use several statistical indicators, including R², root mean square error (RMSE), mean absolute error (MAE), r between observed and predicted values, and regression coefficients between observed and predicted values (Kim et al., 2021; Li and Wu, 2021; Liu et al., 2017). Hence we also apply these indicators to evaluate the estimation accuracy of the GWPR model. R² is a critical statistical indicator describing the goodness of fit. A high R² in the models means that the discrepancy between the predicted NO₂ concentration and the measured ground-level NO₂ concentration is small. The R² calculation is as follows:

$$R^2 = 1 - \frac{\sum_{k=1}^n (MNO2_k - PNO2_k)^2}{\sum_{k=1}^n (MNO2_k - \bar{MNO2})^2} \quad (17)$$

where n represents the observation number in the total sample, $MNO2_k$ represents the k th record of the measured ground-level NO₂ concentration, $PNO2_k$ represents the k th record of the predicted NO₂ concentration, and $\bar{MNO2}$ represents the mean of the measured ground-level NO₂ concentration. It must be noted that this R² of the GWR or the GPWR is the global value because here the total sample is used. The

RMSE is also calculated, indicating the differences between the predicted NO₂ concentration and the measured ground-level NO₂ concentration. The RMSE is sensitive to both systematic error and random error, shown as follows:

$$RMSE = \sqrt{\frac{1}{n} \sum_{k=1}^n (MNO2_k - PNO2_k)^2} \quad (18)$$

The MAE is calculated as follows:

$$MAE = \text{mean}(|MNO2_k - PNO2_k|) \quad (19)$$

In the analysis, the MAE should be low. Additionally, the regression coefficients between observed and predicted values are imputed as follows:

$$MNO2_k = \alpha + \beta PNO2_k + \delta_k \quad (20)$$

where α is the intercept in the regression and the ideal value of α is 0, β is the slope and its ideal value is 1, and δ_k is a random error term.

2.2.4. Spatial interpolation of the coefficients

We use the ordinary kriging (OK) method, described in a previous study (Li and Heap, 2011), to interpolate the coefficients of the GWPR result into raster data. Directly using the GWPR result is insufficient to predict and obtain the ground-level NO₂ concentration raster data because the result is a spatial point data frame and the coefficients vary spatially. There are several reasons for employing the OK method. First, kriging methods can obtain relatively high accuracy when the interpolation covers a large spatial scope (Bivand et al., 2008). Second, for each interpolation, it is valid that the variogram model is the same on an even global scale. Third, the interpolated data are spatially isotropic. Fourth, we interpolate the local coefficients from the GWPR result, whose mean and variance are constant across the spatial field. The general form of the OK method is expressed (Pebesma, 2004) as follows:

$$\hat{\beta}(s_0) = \sum_{l=1}^m \lambda_l \beta(s_l) \text{ with } \sum_{l=1}^m \lambda_l = 1 \quad (21)$$

where $\hat{\beta}(s_0)$ represents the coefficient at unobserved location s_0 , $\beta(s_l)$ represents the coefficient value at known location s_l , λ_l is the spatial weight for the coefficient value at the l th location, and m is the number of known values. To obtain the optimal λ_l , there are two requirements in OK: unbiased and minimal variance of estimation. If $\sum_{l=1}^m \lambda_l$ is equal to 1, then it is unbiased (Pebesma, 2004). To minimize the estimation variance, we use the spherical semivariance mathematical model. Harnessing the OK method, the GWPR results would be estimated to several coefficient raster data with a 0.25-arc-degree spatial resolution. Additionally, the mean value raster data of variables are also interpolated by the OK method. In the prediction process, the data transformations following Eqs. 12 and 13 are necessary. To check the reliability of the interpolation process, we apply leave-one-out cross validation. Simply stated, leave-one-out cross-validation requires that the number of folds equals the number of cities in our dataset. In the cross validation process, one specific city is selected as the test set, while all 529 other cities are used as the training set. This process will repeat 530 times until each city has been selected as the test set.

2.2.5. Predictions of ground-level NO₂ concentration and change trends

The monthly global ground-level NO₂ concentration raster data are predicted based on the original raster data, coefficient rasters, and mean value rasters, following Eq. 15. Furthermore, because the ground-level NO₂ concentration cannot be negative, any value less than zero is set to zero in the prediction grid data. The prediction process creates 82-month grid data. To detect the monthly change trends of each grid, the monthly NO₂ concentrations of each grid are regressed with their month order. The first month of our dataset is January 2015, so the month order of data in January 2015 is the 1st. The month order of

October 2021 is 82nd. The monthly change trends are estimated as follows:

$$PNO2_{LT} = \alpha_L + \beta_L MO_T + \varphi_{LT} \quad (22)$$

where $PNO2_{LT}$ is the predicted NO_2 concentration in grid L in the T th month, MO_T is the month order of $PNO2_{LT}$, α_L is the intercept in grid L , β_L is the monthly NO_2 concentration change trend in grid L , and φ_{LT} is a random error term. It must be noted that the data from a certain grid should be subjected to the regression once if there are no <30 records. Additionally, every individual regression uses only the data from one grid.

3. Results

3.1. Validation of the GWPR Results

The overall accuracy of the GWPR based on FEM is 74.45%, the RMSE is $7.171 \mu\text{g}/\text{m}^3$, and the MAE is $3.48 \mu\text{g}/\text{m}^3$. The mean globally measured ground-level NO_2 is $19.47 \mu\text{g}/\text{m}^3$. Fig. 9 shows the relationship between the predicted and measured ground-level NO_2 concentrations in the GWPR, and all coefficients in Fig. 9 are significant. The coefficient of the correlation (r) between the predicted and measured values is 0.863, following Eq. 4, i.e., there is a strong correlation. Furthermore,

the OLS regression between measured and predicted values also illustrates the significant relationship since the slope is approximately 1.021 significantly, and the ideal value is 1. To confirm whether the goodness of fit of a specific year is apparently lower than that of other years, we calculate all the yearly statistical indicators. In Table 1, the yearly statistical indicators, including R^2 , RMSE, correlation coefficient (r), the slope and intercept of regressions between measured and predicted values, are listed. The lowest yearly R^2 is 51.54% in 2021. The yearly RMSE and MAE peak in 2021 and 2018, respectively, which are 9.619

Table 1
Yearly statistical indicators summary of the GWPR results.

Year	N	R^2	RMSE ($\mu\text{g}/\text{m}^3$)	MAE ($\mu\text{g}/\text{m}^3$)	r	Slope	Intercept
2015	3115	86.46%	5.151	3.476	0.930	0.843	3.623
2016	3315	81.64%	6.126	3.617	0.904	0.794	4.508
2017	2936	85.20%	5.442	3.355	0.925	0.803	4.242
2018	3560	74.99%	8.881	4.071	0.869	0.689	6.461
2019	5790	71.34%	7.475	3.566	0.846	0.676	6.418
2020	6023	77.32%	5.317	3.335	0.881	0.827	2.912
2021	4947	51.55%	9.619	3.115	0.718	0.520	7.831
Total	29,686	74.45%	7.171	3.480	0.863	0.724	5.373

Note: The Ideal value of slope is 1, and the ideal value of intercept is 0.

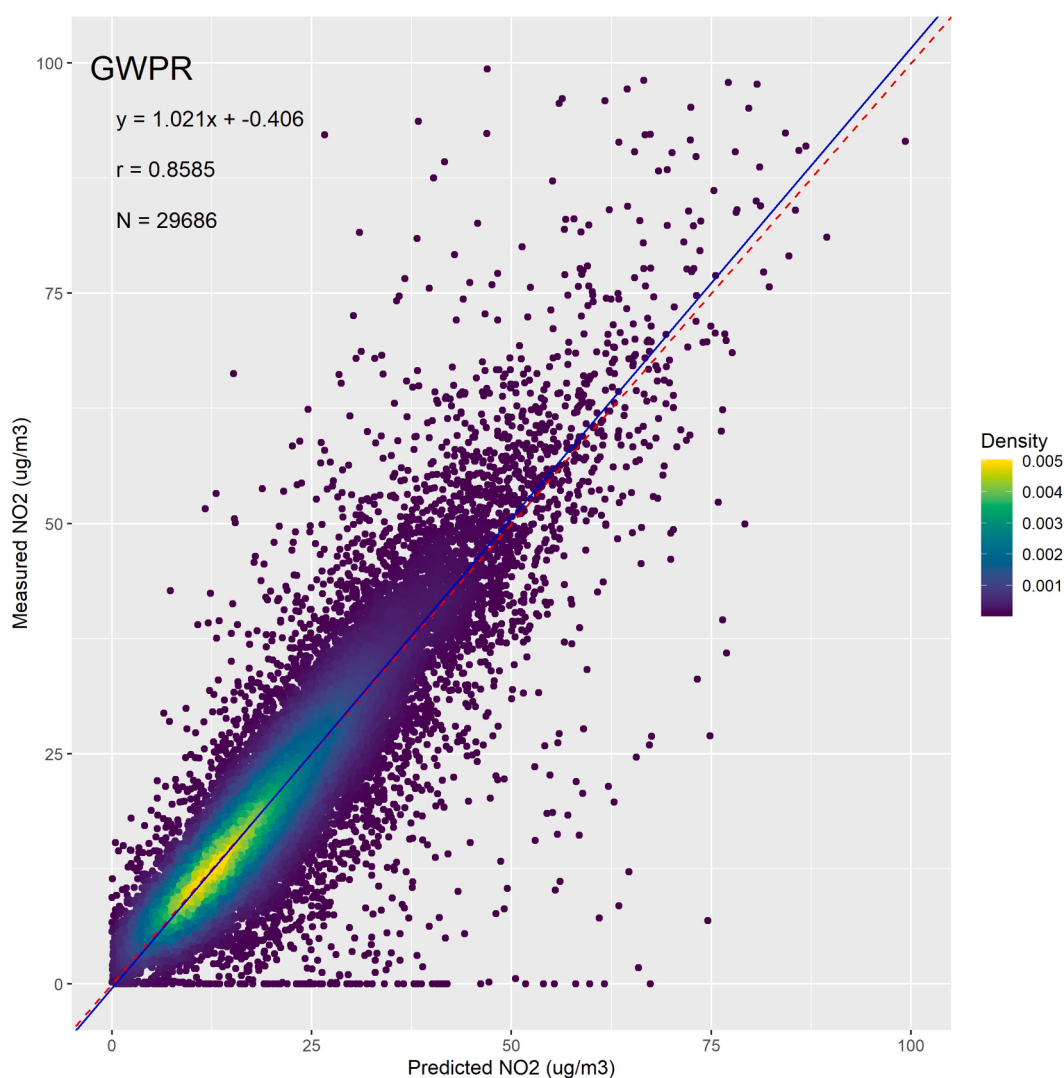


Fig. 9. The density plots between the measured ground-level NO_2 concentration and the predicted NO_2 concentration from the GWPR results. (The red dashed line is the 1:1 line. The blue line is the regression line.)

and $4.071 \mu\text{g}/\text{m}^3$. In September 2021, the measured ground-level NO₂ concentration in Puebla, a Mexican city, suddenly increased to >20 times the usual level. In October 2021, the data of this city were missing. As we mentioned in the Materials section, this seemingly strange record also causes the high skewness of the measured ground-level NO₂ concentration distribution. The available daily data in that city are close to its monthly average value in September 2021. Thus, we keep that record in the analysis. However, if we ignore this individual record, the R² in 2021 will reach 78.10%. Comparisons of monthly time series illustrate that the GWPR captures the monthly temporal variability accurately (Fig. 10).

Table 2 reports the results of 10-fold cross validation. The total dataset is randomly divided into ten subsets. In every single cross validation, nine subsets are used to train the model. Then the reserved subset and the coefficients from the trained model are employed to predict the dependent variable. The performance of the GWPR based on FEM is stable in terms of goodness of prediction for the test subsets. The lowest prediction accuracy for the test subset is 68.55%, and its RMSE, MEA, and coefficient (*r*) of the correlation between the predicted and measured values are $15.569 \mu\text{g}/\text{m}^3$, $4.399 \mu\text{g}/\text{m}^3$, and 0.627, respectively. The 10-fold cross validation results show the reliability of the GWPR model.

3.2. Validation of the OK interpolations

Table 3 illustrates the result of the leave-one-out cross validation of the coefficient and mean value interpolations. The worst performance of the OK method is from the interpolation of the mean value of measured ground-level NO₂, whose R² is 34.50%, but its RMSE and MAE are not high, which are $7.773 \mu\text{g}/\text{m}^3$ and $5.633 \mu\text{g}/\text{m}^3$, respectively. For the low RMSE and MAE values, this interpolated grid dataset is still acceptable. There is a new indicator named on point R² in **Table 3**. This indicator depicts how much the observed values change after interpolation. In the OK method, the spatial weight might not equal 1 when the distance between two points equals 0, i.e., they overlap. Hence, after OK interpolation, the predicted values from the imputed grid dataset might differ slightly from the observed values. The on-point R² indicates that none of the interpolations lose the accuracy of $>2\%$, and most of them only slash the accuracy by 0.1%.

3.3. Prediction and monthly change trends

The accuracy of the predicted grid dataset is 69.61%, and the RMSE and MAE are $7.82 \mu\text{g}/\text{m}^3$ and $4.07 \mu\text{g}/\text{m}^3$, respectively. Due to the slight change in the interpolation process, the accuracy of the final prediction is lower than that of the GWPR result. **Fig. 11** demonstrates the relationship between the predicted and measured ground-level NO₂ concentrations in the predicted grid datasets, and all coefficients in **Fig. 11** are significant. The *r* is 0.838, which is lower than the *r* in the GWPR result (0.859). According to the tiny difference of all statistical indicators between the GWPR result and the grid data prediction result, the final prediction data are reasonable.

Fig. 12 presents the average monthly ground-level NO₂ concentration. The results show that the ground-level NO₂ concentration in Asia is relatively higher than that in other continents. Moreover, in western Asia, the ground-level NO₂ pollution is the most severe. In most regions of Iran, Iraq, and Turkmenistan, the average values even exceed $100 \mu\text{g}/\text{m}^3$. It is much higher than WHO's ambient NO₂ concentration limits, which is an annual mean of $40 \mu\text{g}/\text{m}^3$ in link with previous studies (Kasparoglu et al., 2018; Yousefian et al., 2020). Moreover, some regions in northern China, India, Chile, Bolivia, South Africa, northern Italy, and the west coast of the United States are also severely polluted. This is consistent with previous research (Di et al., 2020; Kim et al., 2021; Zheng et al., 2019). Moreover, in **Fig. 12**, we plot 110 main cities' average measured ground-level NO₂ concentrations from January 2015 to October 2021. The measured values are consistent with our

predictions. The map of average monthly ground-level NO₂ concentrations without city points and monthly ground-level NO₂ concentrations from January 2015 to October 2021 are shown in the **Supplementary Materials** (Figs. S1 – S83). **Fig. 13** shows the average monthly TrCA of the NO₂ concentration from January 2015 to October 2021. There are some differences between the two spatial distributions. As assumed, the relationship between the TrCA of NO₂ and the ground-level NO₂ spatially varies. Thus, the same amounts of NO₂ in the troposphere might contribute disproportionately to the ground-level NO₂ concentration in the different places. **Fig. 14** displays the monthly trends of the means of predicted ground-level NO₂ concentrations in all the grids and the cities with the measurements. Both the mean values of all the global grids and the cities with measurements show downward trends. The monthly change trends of each grid and the means of all the global grids and the cities with measurements are estimated following Eq. 20. The slope of the regression between the average ground-level NO₂ concentration of the cities and month order is -0.097 (95% confidence interval: -0.140 - -0.053 , *p* value $<0.1\%$), indicating an approximately 0.097 (95% CI: 0.053 – $0.140 \mu\text{g}/\text{m}^3$) decrease per month from January 2015 to October 2021. Moreover, the mean of all the grids decreases by approximately 0.066 (95% CI: 0.033 – $0.099 \mu\text{g}/\text{m}^3$ (*p* value $<0.1\%$) per month. **Fig. 15** illustrates the monthly change trends of each grid. All the values shown in **Fig. 15** should be significant at the 0.1 level. **Fig. 15** demonstrates that the ground-level NO₂ concentration gradually decreases in most regions. However, in the Red Sea region, Arabian Peninsula, Persian Gulf, the ground-level NO₂ concentration is increasing, even though these are already the most severely polluted areas. In addition, the changes in most places in India and Mexico also show an upward trend. In some areas of California and Nevada in the United States too, the change trends are increasing.

4. Discussion

We employ the GWPR model to examine the association of satellite-derived data with measured ground-level NO₂ concentrations from January 2015 to October 2017 among 530 cities. The accuracies of the GWPR (74.45%) and raster prediction (69.61%) exceed most previous studies on regional ground-level NO₂ concentrations (Kim et al., 2021; Li et al., 2020; Qin et al., 2017). Our analysis provides the first example of the GWPR on an unbalanced panel dataset. Our study predicts 82 monthly global ground-level NO₂ concentrations with a 0.25-arc-degree spatial resolution from January 2015 to October 2021 (shown in the **Supplementary Materials**). Additionally, our analysis demonstrates the monthly change trends of each grid.

In terms of accuracy, our study has made some improvements in the ground-level NO₂ concentration estimation based on the satellite dataset. The accuracy of a study on ground-level NO₂ concentrations over Central-Eastern China employing GTWR is 0.60, which is lower than our 0.70 (Qin et al., 2017). Additionally, its MEA is $9.28 \mu\text{g}/\text{m}^3$, while our MEA is $5.633 \mu\text{g}/\text{m}^3$. A study over the Wuhan urban agglomeration applying space-time neural networks obtained 0.69 accuracy and an $8.29 \mu\text{g}/\text{m}^3$ RMSE, while our RMSE was $7.82 \mu\text{g}/\text{m}^3$ (Li et al., 2020). Additionally, a study over Switzerland and northern Italy using machine learning technology provides a 59%-accuracy prediction, and its MEA is $7.69 \mu\text{g}/\text{m}^3$ (Kim et al., 2021). However, these studies excel at either spatial or temporal resolution.

The spatial distribution and concentrations of the predictions are compared with previous studies. According to a study by Di et al., in the metropolitan areas of Michigan, Illinois, Wisconsin, New England, Colorado, Nevada and California, NO₂ pollution is at harmful levels, higher than 25 PPB (Di et al., 2020). Our prediction is in line with this study since the ground-level NO₂ in those places is predicted to be approximately $40 \mu\text{g}/\text{m}^3$ (under an ambient pressure of 1 atm and a temperature of 25°C , 1 PPB NO₂ roughly equals $1.88 \mu\text{g}/\text{m}^3$). Kasparoglu et al. proposed that in urban sites of the Marmara regression of Turkey, the NO₂ concentrations were higher than $75 \mu\text{g}/\text{m}^3$ (Kasparoglu et al.,

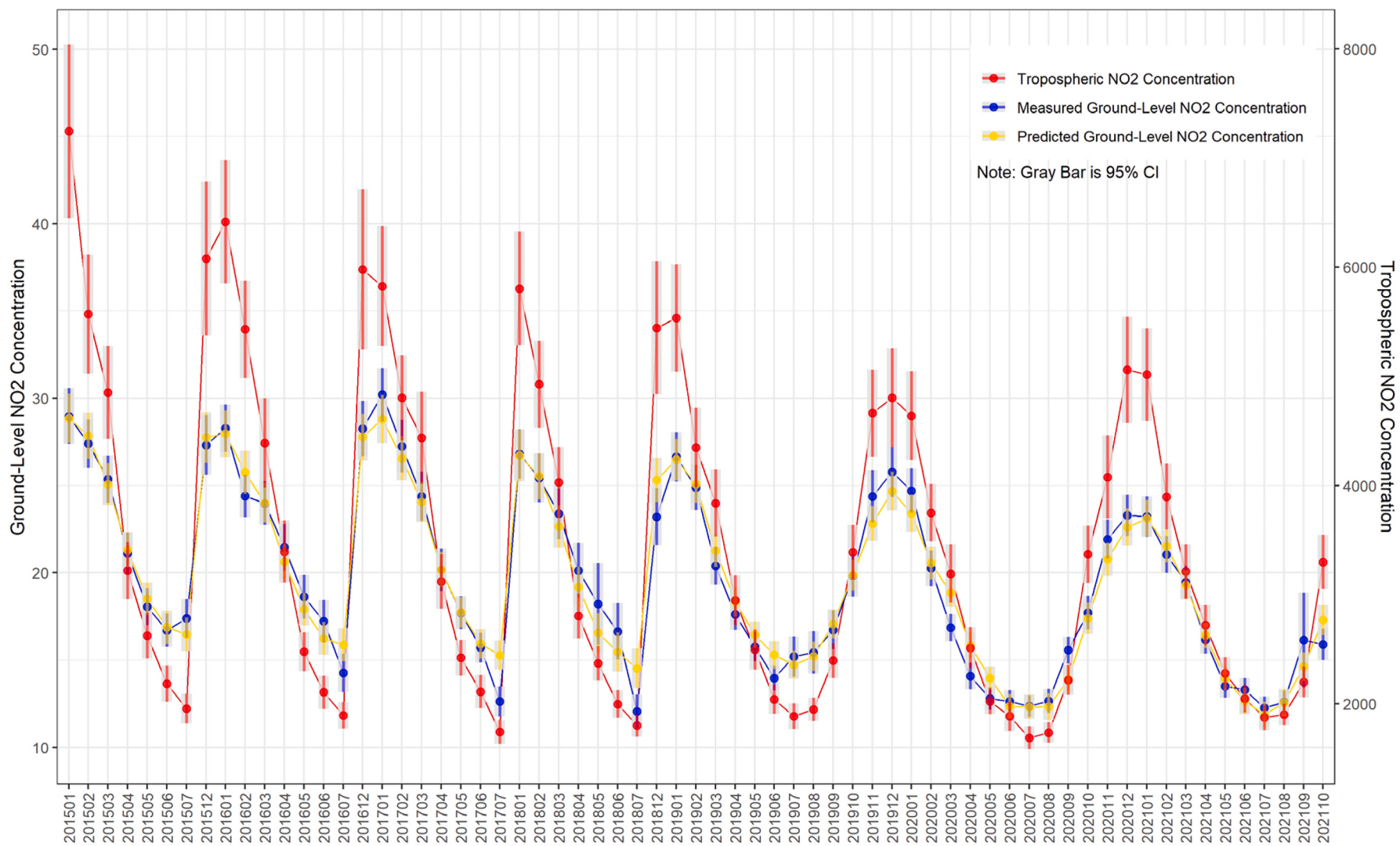


Fig. 10. Time series comparisons of monthly means of tropospheric, measured ground-level, predicted ground-level NO₂ concentration and their 95% confidence interval. (Unit: tropospheric NO₂ concentration [$\mu\text{g}/\text{m}^2$], measured and predicted Ground-level NO₂ concentration [$\mu\text{g}/\text{m}^3$])

Table 2

Statistical indicators summary of 10-fold cross validation.

	Statistical Indicator of Training						Statistical Indicator of Testing							
	N	R2	RMSE $\mu\text{g}/\text{m}^3$	MAE $\mu\text{g}/\text{m}^3$	r	Slope	Intercept	N	R2	RMSE $\mu\text{g}/\text{m}^3$	MAE $\mu\text{g}/\text{m}^3$	r	Slope	Intercept
1	26,718	89.68%	7.746	3.800	0.839	0.681	6.195	2968	89.73%	7.669	4.096	0.831	0.691	6.139
2	26,718	89.47%	7.843	3.861	0.837	0.684	6.151	2968	89.90%	7.422	4.367	0.825	0.733	5.296
3	26,718	89.54%	7.828	3.846	0.839	0.683	6.148	2968	91.42%	6.754	3.994	0.844	0.799	4.160
4	26,718	92.53%	6.464	3.719	0.876	0.749	4.926	2968	68.55%	15.57	4.399	0.627	0.358	12.275
5	26,718	89.96%	7.640	3.763	0.844	0.692	6.009	2968	91.02%	7.155	4.055	0.854	0.711	5.592
6	26,718	90.04%	7.637	3.828	0.847	0.694	5.960	2968	90.13%	7.267	4.025	0.826	0.793	4.044
7	26,718	89.61%	7.777	3.790	0.839	0.681	6.226	2968	92.39%	6.546	3.997	0.875	0.762	4.511
8	26,718	90.55%	7.404	3.724	0.853	0.705	5.756	2968	89.39%	7.875	4.171	0.834	0.683	6.137
9	26,718	90.95%	7.268	3.742	0.862	0.712	5.602	2968	89.98%	7.418	4.160	0.828	0.781	4.391
10	26,712	90.27%	7.515	3.759	0.849	0.693	5.976	2974	90.76%	7.332	4.086	0.856	0.710	5.718

Note: The Ideal value of slope is 1, and the ideal value of intercept is 0. When the values of statistical indicators are close between training results and testing result, the predictions of model are reliable.

Table 3

Statistical indicators summary of the leave-one-out cross validation of OK interpolation.

	Variable	N	R ²	MRSE $\mu\text{g}/\text{m}^3$	MAE $\mu\text{g}/\text{m}^3$	r	Intercept	Slope	On Point R ²
Coefficient Interpolation	TrCA of NO ₂	530	67.54%	8.49E-04	3.81E-04	0.826	-9.31E-05	1.109	99.87%
	Terrain Atmospheric Pressure	530	77.99%	0.148	0.079	0.883	0.003	1.021	99.86%
	Temperature	530	60.11%	0.320	0.102	0.778	0.015	1.080	99.91%
	NDVI	530	79.28%	16.815	6.491	0.892	1.065	1.053	99.93%
	Precipitation	530	75.46%	14.210	5.288	0.869	0.682	1.037	99.91%
	PBLH	530	72.38%	0.004	0.002	0.852	0.001	1.054	99.83%
	2016 Year	530	72.38%	0.004	0.002	0.852	0.001	1.054	99.85%
	2017 Year	530	71.89%	3.161	1.378	0.848	0.081	1.021	99.87%
	2018 Year	530	55.09%	6.727	1.986	0.743	0.218	1.009	99.83%
	2019 Year	530	72.50%	3.642	1.555	0.852	0.150	1.028	99.87%
Mean Value Interpolation	2020 Year	530	75.28%	3.273	1.443	0.868	0.170	1.013	99.87%
	2021 Year	530	76.82%	3.791	1.643	0.877	0.223	1.029	99.87%
	Measured Ground-Level NO ₂	530	34.50%	7.773	5.633	0.626	4.505	0.748	98.40%
	TrCA of NO ₂	530	79.85%	1143.454	738.228	0.896	75.632	0.946	99.59%
	Terrain Atmospheric Pressure	530	67.70%	36.269	21.535	0.823	-17.663	1.018	99.79%
	Temperature	530	84.21%	2.597	1.564	0.919	-0.821	1.046	99.92%
	NDVI	530	54.86%	0.095	0.068	0.748	0.059	0.876	99.44%
	Precipitation	530	86.86%	0.022	0.012	0.932	-0.002	1.009	99.94%
	PBLH	530	77.98%	101.276	53.343	0.883	-18.025	1.024	99.91%

2018), consistent with our study. Yousefian et al. proposed that during 2012–2017, the NO₂ concentration in Tehran, the capital of Iran, was always 1.5–2.5 times higher than WHO limits (40 $\mu\text{g}/\text{m}^3$) (Yousefian et al., 2020), which was also the most polluted area in our research. Kim et al.'s research hints that in an alpine domain, the NO₂ in urban regions is always over 40 $\mu\text{g}/\text{m}^3$ (Kim et al., 2021), which is in keeping with our study. Additionally, Chi et al. estimated the annual average ground-level NO₂ concentration in the main regions of China over 2014–2020 (Chi et al., 2021). Its results are similar to our predictions. Moreover, because research on the ground-level NO₂ concentration in polar regions is rare, it is difficult to compare our study with previous studies. However, the low temperature and PBLH might account for the high NO₂ concentration in polar regions. Evidence shows that in winter, the NO₂ concentration is apparently higher than it is in summer (Fan et al., 2020; Shen et al., 2021; Yousefian et al., 2020). PBLH is negatively related to ground-level air pollution (Xiang et al., 2019). To summarize, our study is in line with the most recent studies on ground-level NO₂ concentrations.

It must be underscored that the spatial distributions of the ground-level NO₂ concentration and TrCA of NO₂ are different, as Figs. 12 and 13 show. Put another way, the impacts of the TrCA of NO₂ on the ground-level NO₂ concentration vary spatially. Fig. 3.a illustrates the discrepancy between the TrCA of NO₂ and the ground-level NO₂ concentration. For example, some points with no >1000 $\mu\text{g}/\text{m}^2$ TrCA of NO₂ have a >60 $\mu\text{g}/\text{m}^3$ ground-level NO₂ concentration. The potential reason for this is that most NO₂ in a certain column distributes near the surface,

although the total amount of NO₂ in this column is small. Moreover, several other points with >20,000 $\mu\text{g}/\text{m}^2$ TrCA of NO₂ have a less-than-30- $\mu\text{g}/\text{m}^3$ ground-level NO₂ concentration. In this case, there is a large amount of NO₂ molecules in a specific column, but most of them might be hundreds of meters away from the surface. Several geoengineering measures could drive air pollution to penetrate the planetary boundary layer into the troposphere to avoid clustering at the surface (Liu et al., 2021). Ground-level atmospheric monitoring equipment cannot detect these NO₂ molecules, even though emissions might be high there. Because the physical and chemical properties of the atmosphere affected by geographical and environmental factors are not the same everywhere, we employ GWPR to predict the ground-level NO₂ concentration rather than use other global models to estimate it directly. The spatially varied relationship between the TrCA of NO₂ and the ground-level NO₂ concentration is the main reason leading to the difference between Figs. 12 and 13.

Our monthly grid data demonstrate that the temporal variation in the spatial distribution of the ground-level NO₂ concentration is evident (shown in Supplementary Materials and Fig. 10). In December, January, and February, the NO₂ pollution over the Northern Hemisphere is relatively serious, while it is high in June, July, and August over the Southern Hemisphere. The possible reasons for this temporal variation are as follows: first, NO₂ can last longer, or it is difficult to be removed in a low-temperature environment (Yousefian et al., 2020); second, residential energy use for heating might produce more NO₂ (Fan et al., 2020); and third, the low temperature changes other meteorological

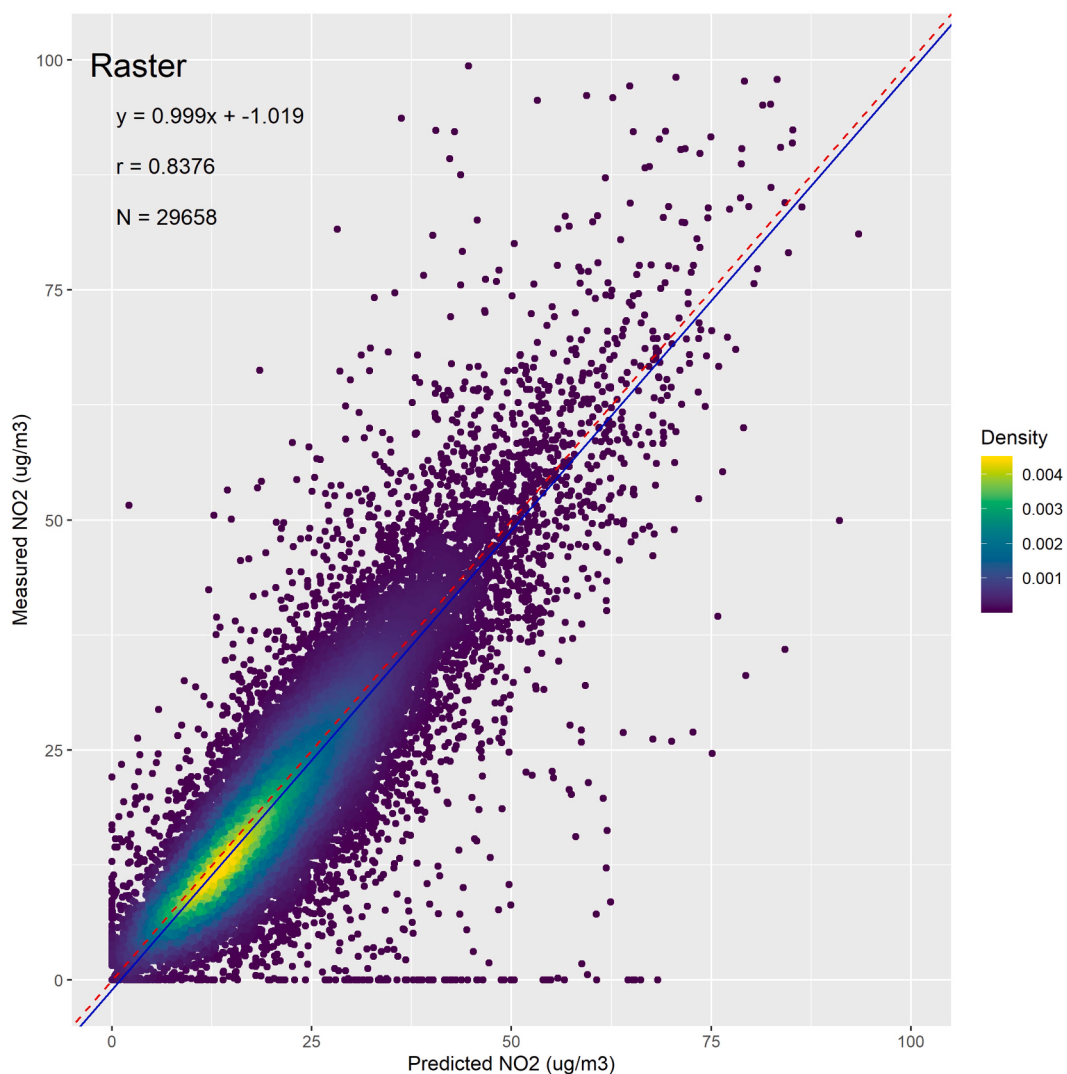


Fig. 11. The density plots between the measured ground-level NO₂ concentration and the predicted NO₂ concentration from the predicted grid datasets. (The red dashed line is the 1:1 line. The blue line is the regression line.)

factors that eventually leads to NO₂ being unable to spread to other zones far from the surface (Fan et al., 2020; Shen et al., 2021). However, no matter what the main reason is, policy-makers should take this temporal variation into account when devising air pollution policies.

Some limitations remain in our study. First, the number of measurement points is limited, and their spatial distribution is unbalanced. Our dataset takes only 530 cities into account globally without considering rural areas. Especially in Africa and South America, there are few measurement points. Second, the spatial resolutions of one control variable, namely, PBLH, are not good enough. Third, some hidden variables are ignored. For instance, the research does not involve the impacts of air pollution policies and COVID-19, although we have used year dummy variables to reduce their effects. Fourth, the spatial and temporal resolutions are relatively low. Future studies should focus on the following topics. First, the GWPR model should be further optimized. For example, if the dataset contains data islands based on a certain bandwidth, whether the GWPR is still statistically reliable remains unknown. Second, more confounders, such as land cover and human activity, among others, need to be included in future analyses. Finally, the vertical distribution of NO₂ in air and its physical and chemical causes should be carefully explored. Third, the vertical distribution of air pollutants in the atmosphere in different places should be probed and analyzed.

5. Conclusions

This study creates a GWPR model to detect the spatial variation in the relationship between the measured ground-level NO₂ concentration and satellite-derived data. It predicts the monthly ground-level NO₂ concentration based on the data from the OMI and other satellite platforms. The GWPR model exhibits outstanding accuracy (74.45%), r value (0.863), RMSE ($7.171 \mu\text{g}/\text{m}^3$) and MAE ($3.480 \mu\text{g}/\text{m}^3$) in the estimation and stability in the cross validation. The GWPR is a simple but effective model to estimate monthly global ground-level NO₂ concentrations at a 0.25-degree spatial resolution. The predictions provide critical basic data to environmental and public health science and valuable information for governments and societies to formulate more reasonable and efficient policies.

Data availability

All data sources used in the analyses, along with fully reproducible code, are publicly available at https://github.com/MichaelChaoLi-cpu/Monthly_Global_Ground_Level_NO2. The predicted data from January 2015 to October 2021 and the animation of ground-level NO₂ concentration could also be found in the abovementioned websites.

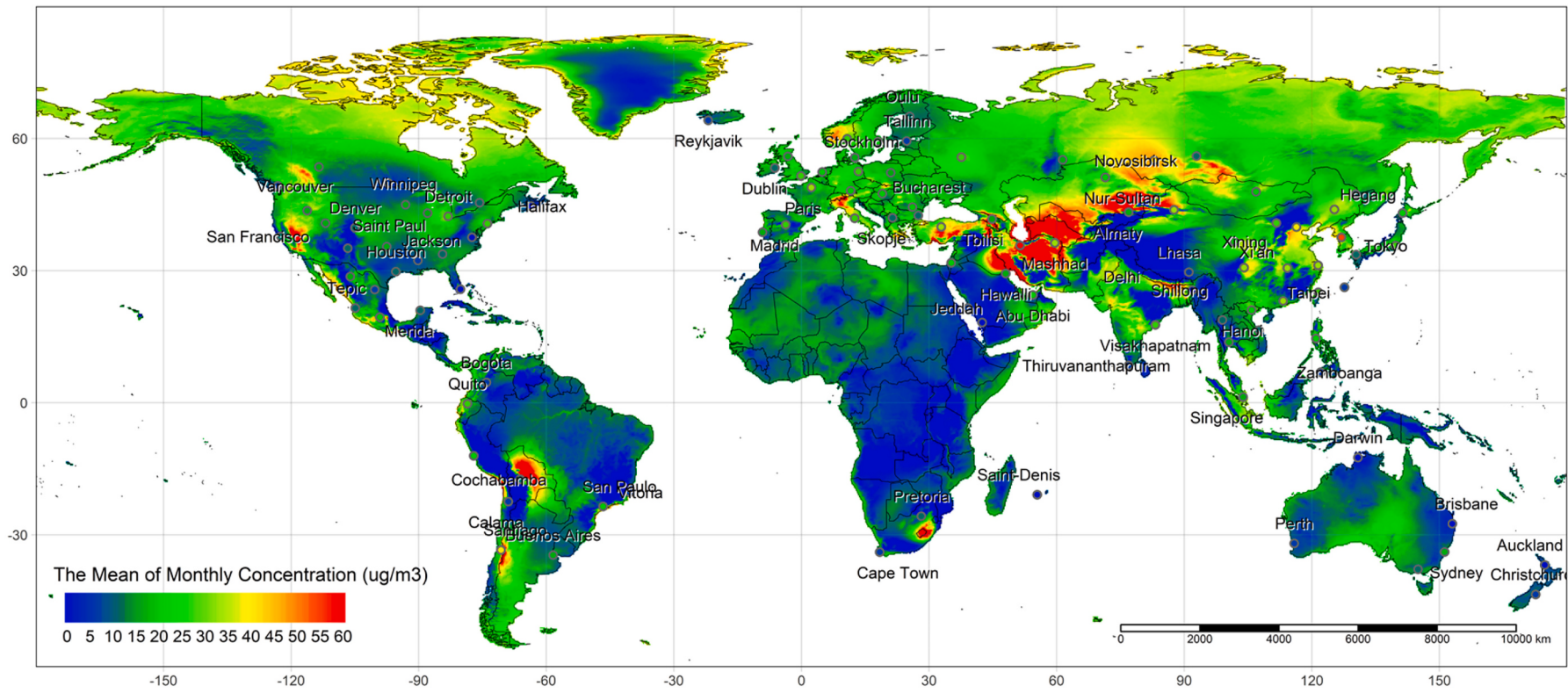


Fig. 12. Map of average monthly ground-level NO_2 concentration ($\mu\text{g}/\text{m}^3$), Jan 2015 – Oct 2021.

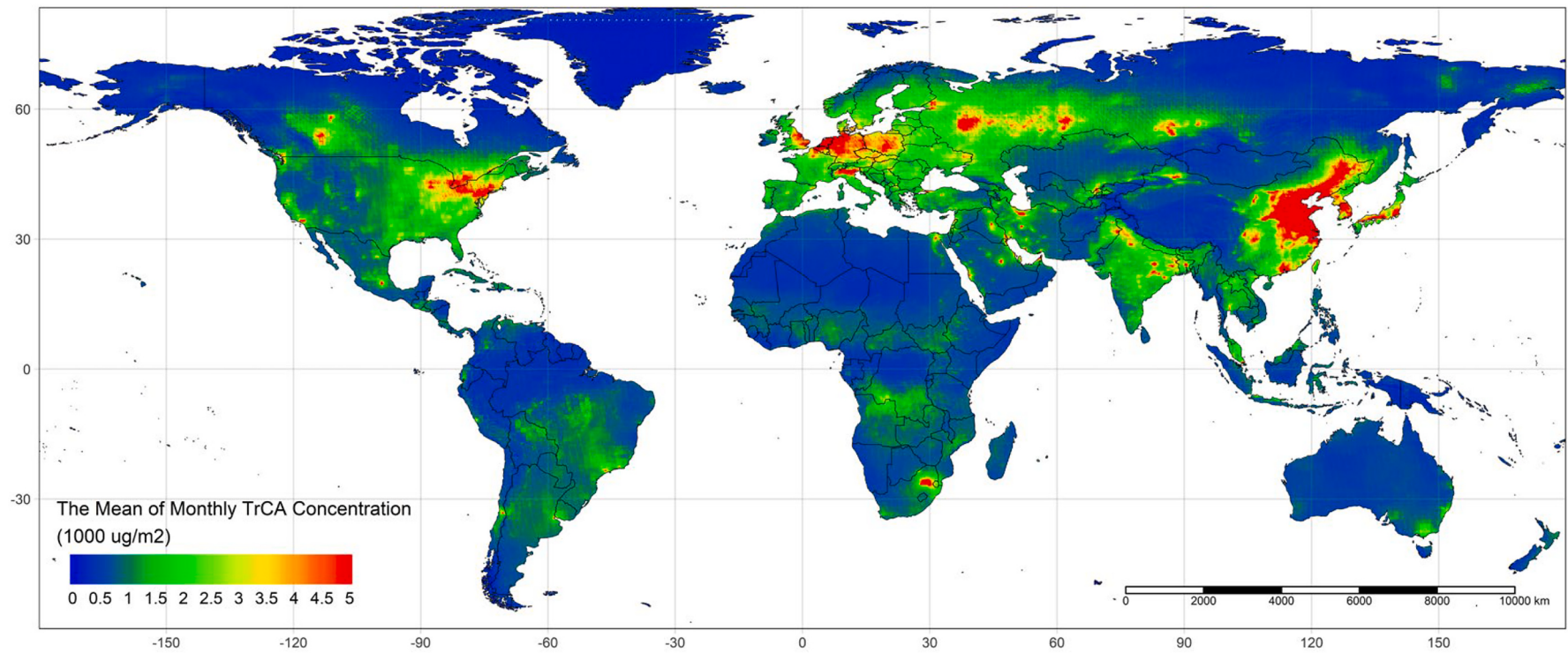


Fig. 13. Map of average monthly TrCA NO₂ concentration ($1000 \mu\text{g}/\text{m}^2$), Jan 2015 – Oct 2021.

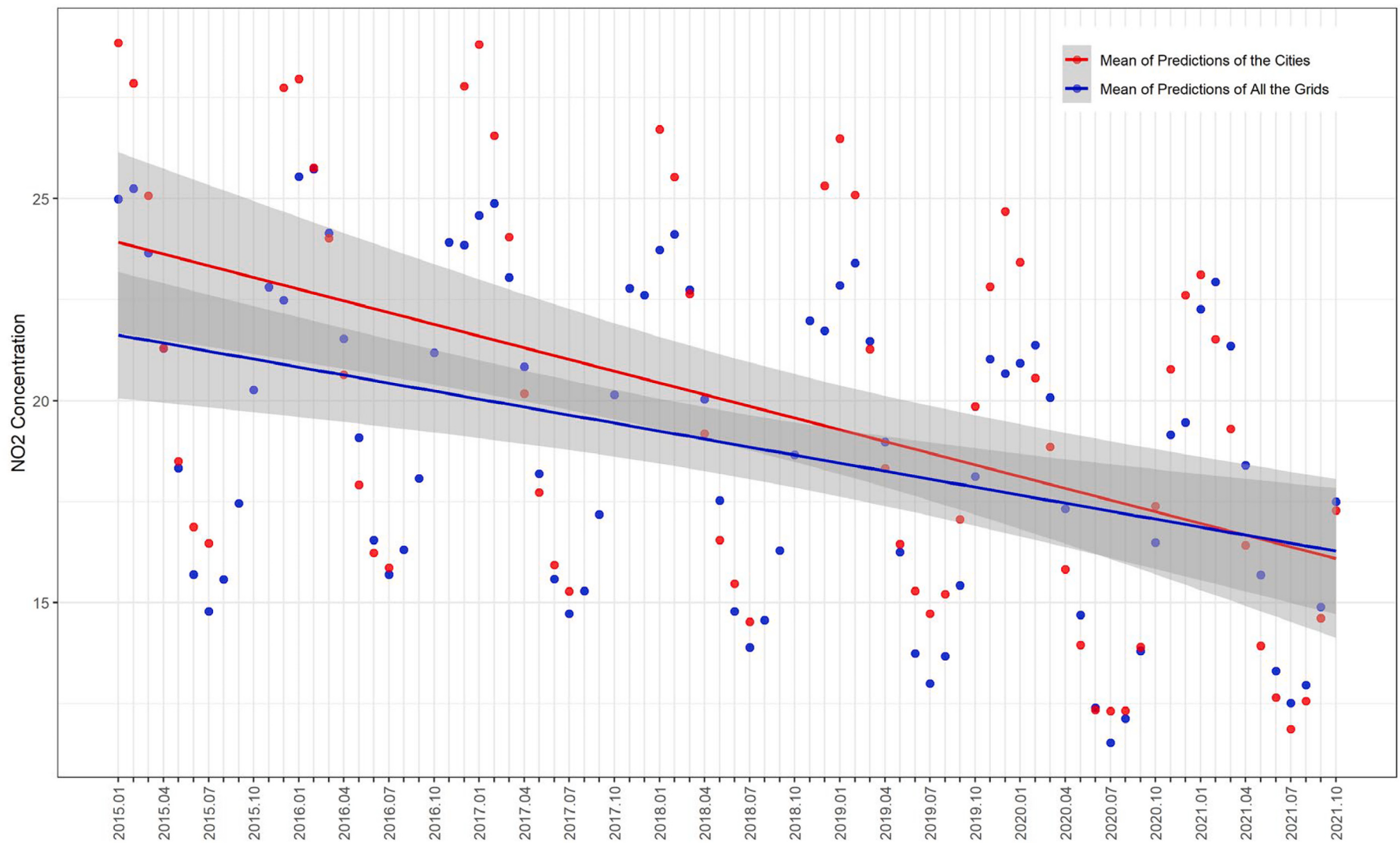


Fig. 14. Monthly change trends of average predicted ground-level NO₂ concentration ($\mu\text{g}/\text{m}^3$), Jan 2015 – Oct 2021.

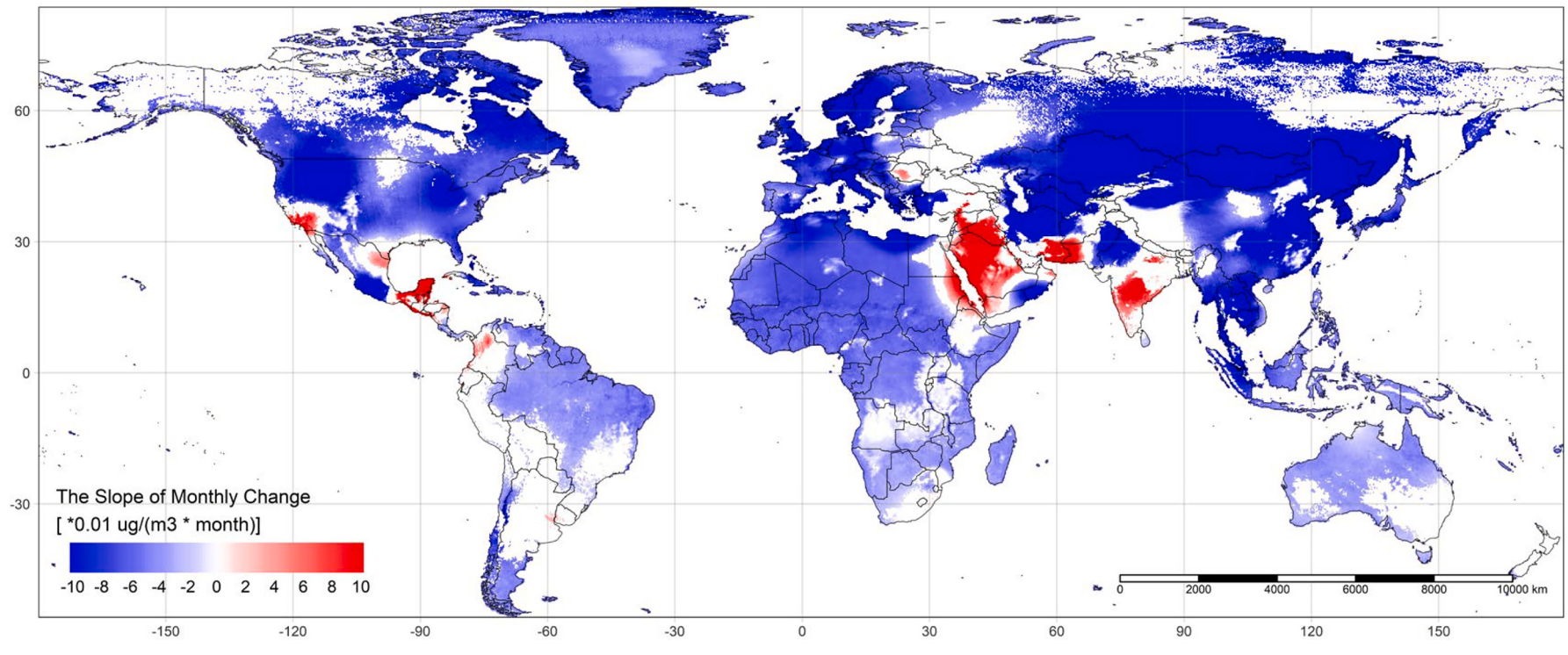


Fig. 15. Map of monthly change trends of ground-level NO₂ concentration ($0.01 \mu\text{g}/(\text{m}^3 \times \text{month})$), Jan 2015 – Oct 2021.

CRediT authorship contribution statement

Chao Li: Conceptualization, Methodology, Software, Validation, Formal analysis, Investigation, Data curation, Writing – original draft, Visualization. **Shunsuke Managi:** Resources, Writing – review & editing, Supervision, Project administration, Funding acquisition.

Declaration of Competing Interest

The authors declare that they have no known competing financial interests or personal relationships that could have appeared to influence the work reported in this paper.

Acknowledgments

The authors gratefully acknowledge all the support, financial or otherwise, in enabling the work here to be carried out. This research was supported by the following funding agencies: JSPS KAKENHI (Grant No. JP20H00648), the Environment Research and Technology Development Fund of the Environmental Restoration and Conservation Agency of Japan (Grant No. JPMEERF20201001), and also JST SPRING (Grant No. JPMJSP2136).

Appendix A. Supplementary data

Supplementary data to this article can be found online at <https://doi.org/10.1016/j.rse.2022.113152>.

References

- Bechle, M.J., Millet, D.B., Marshall, J.D., 2015. National spatiotemporal exposure surface for NO₂: monthly scaling of a satellite-derived land-use regression, 2000–2010. *Environ. Sci. Technol.* 49, 12297–12305.
- Beckerman, B., Jerrett, M., Brook, J.R., Verma, D.K., Arain, M.A., Finkelstein, M.M., 2008. Correlation of nitrogen dioxide with other traffic pollutants near a major expressway. *Atmos. Environ.* 42, 275–290.
- Beenstock, M., Felsenstein, D., 2019. The Econometric Analysis of Non-Stationary Spatial Panel Data. Springer.
- Bigdeli, M., Taheri, M., Mohammadian, A., 2021. Spatial sensitivity analysis of COVID-19 infections concerning the satellite-based four air pollutants levels. *Int. J. Environ. Sci. Technol.* 18, 751–760.
- Bivand, R.S., Pebesma, E.J., Gómez-Rubio, V., Pebesma, E.J., 2008. Applied Spatial Data Analysis with R. Springer.
- Breusch, T.S., Pagan, A.R., 1980. The lagrange multiplier test and its applications to model specification in econometrics. *Rev. Econ. Stud.* 47, 239.
- Bruneekreef, B., Holgate, S.T., 2002. Air pollution and health. *Lancet* 360, 1233–1242.
- Brunsdon, C., Fotheringham, S., Charlton, M., 1998. Geographically weighted regression. *J. Roy. Stat. Soc. Ser. D (The Statistician)* 47, 431–443.
- Brunsdon, C., Fotheringham, A.S., Charlton, M.E., 2010. Geographically weighted regression: a method for exploring spatial nonstationarity. *Geogr. Anal.* 28, 281–298.
- Chang, Y., Wang, S., Zhou, Y., Wang, L., Wang, F., 2019. A novel method of evaluating highway traffic prosperity based on nighttime light remote sensing. *Remote Sens.* 12, 102.
- Chi, Y., Fan, M., Zhao, C., Sun, L., Yang, Y., Yang, X., Tao, J., 2021. Ground-level NO₂ concentration estimation based on OMI tropospheric NO₂ and its spatiotemporal characteristics in typical regions of China. *Atmos. Res.* 264, 105821.
- Chiusolo, M., Cadum, E., Stafoggia, M., Galassi, C., Berti, G., Faustini, A., Bisanti, L., Vigotti, M.A., Dessì, M.P., Cerniglio, A., Mallone, S., Pacelli, B., Minerba, S., Simonato, L., Forastiere, F., 2011. Short-term effects of nitrogen dioxide on mortality and susceptibility factors in 10 Italian cities: the EpiAir study. *Environ. Health Perspect.* 119, 1233–1238.
- Croissant, Y., Millo, G., 2008. Panel data econometrics in R: the plm package. *J. Stat. Softw.* 27.
- Curier, R.L., Kranenburg, R., Segers, A.J.S., Timmermans, R.M.A., Schaap, M., 2014. Synergistic use of OMI NO₂ tropospheric columns and LOTOS-EUROS to evaluate the NO_x emission trends across Europe. *Remote Sens. Environ.* 149, 58–69.
- Di, Q., Amini, H., Shi, L., Kloog, I., Silvern, R., Kelly, J., Sabath, M.B., Choirat, C., Koutrakis, P., Lyapustin, A., Wang, Y., Mickley, L.J., Schwartz, J., 2020. Assessing NO₂ concentration and model uncertainty with high spatiotemporal resolution across the contiguous united states using ensemble model averaging. *Environ. Sci. Technol.* 54, 1372–1384.
- Fan, H., Zhao, C., Yang, Y., 2020. A comprehensive analysis of the spatio-temporal variation of urban air pollution in China during 2014–2018. *Atmos. Environ.* 220, 117066.
- Fotheringham, A.S., Oshan, T.M., 2016. Geographically weighted regression and multicollinearity: dispelling the myth. *J. Geogr. Syst.* 18, 303–329.
- Fotheringham, A., Brunsdon, C., Charlton, M., 2002. Geographically Weighted Regression: The Analysis of Spatially Varying Relationships. John Wiley & Sons.
- Fotheringham, A.S., Crespo, R., Yao, J., 2015. Geographical and temporal weighted regression (GTWR). *Geogr. Anal.* 47, 431–452.
- Geddes, J.A., Martin, R.V., Boys, B.L., Van Donkelaar, A., 2016. Long-term trends worldwide in ambient NO₂ concentrations inferred from satellite observations. *Environ. Health Perspect.* 124, 281–289.
- Gollini, I., Lu, B., Charlton, M., Brunsdon, C., Harris, P., 2015. GWmodel: an R package for exploring spatial heterogeneity using geographically weighted models. *J. Stat. Softw.* 63.
- Hamra, G.B., Laden, F., Cohen, A.J., Raaschou-Nielsen, O., Brauer, M., Loomis, D., 2015. Lung cancer and exposure to nitrogen dioxide and traffic: a systematic review and meta-analysis. *Environ. Health Perspect.* 123, 1107–1112.
- Hu, X., Waller, L.A., Al-Hamdan, M.Z., Crosson, W.L., Estes, S.M., Estes, S.M., Quattrochi, D.A., Sarnat, J.A., Liu, Y., 2013. Estimating ground-level PM2.5 concentrations in the southeastern U.S. using geographically weighted regression. *Environ. Res.* 121, 1–10.
- Irie, H., Boersma, K.F., Kanaya, Y., Takashima, H., Pan, X., Wang, Z.F., 2012. Quantitative bias estimates for tropospheric NO₂ columns retrieved from SCIAMACHY, OMI, and GOME-2 using a common standard for East Asia. *Atmos. Measur. Techn.* 5, 2403–2411.
- Jiang, M., Sun, W., Yang, G., Zhang, D., 2017. Modelling seasonal GWR of daily PM2.5 with proper auxiliary variables for the Yangtze river delta. *Remote Sens.* 9, 346.
- Kang, S., 1985. A note on the equivalence of specification tests in the two-factor multivariate variance components model. *J. Econ.* 28, 193–203.
- Kasparoglu, S., Incecik, S., Topcu, S., 2018. Spatial and temporal variation of O₃, NO and NO₂ concentrations at rural and urban sites in Marmara Region of Turkey. *Atmos. Pollut. Res.* 9, 1009–1020.
- Kim, M., Brunner, D., Kuhlmann, G., 2021. Importance of satellite observations for high-resolution mapping of near-surface NO₂ by machine learning. *Remote Sens. Environ.* 264, 112573.
- Larkin, A., Geddes, J.A., Martin, R.V., Xiao, Q., Liu, Y., Marshall, J.D., Brauer, M., Hystad, P., 2017. Global land use regression model for nitrogen dioxide air pollution. *Environ. Sci. Technol.* 51, 6957–6964.
- Lelieveld, J., Evans, J.S., Fnais, M., Giannadaki, D., Pozzer, A., 2015. The contribution of outdoor air pollution sources to premature mortality on a global scale. *Nature* 525, 367–371.
- Li, J., Heap, A.D., 2011. A review of comparative studies of spatial interpolation methods in environmental sciences: performance and impact factors. *Ecol. Informat.* 6, 228–241.
- Li, C., Managi, S., 2021a. Contribution of on-road transportation to PM2.5. *Sci. Rep.* 11, 21320.
- Li, C., Managi, S., 2021b. Spatial variability of the relationship between air pollution and well-being. *Sustain. Cities Soc.* 103447.
- Li, C., Managi, S., 2022. Impacts of air pollution on COVID-19 case fatality rate: a global analysis. *Environ. Sci. Pollut. Res.* Jan 4, 1–14.
- Li, L., Wu, J., 2021. Spatiotemporal estimation of satellite-borne and ground-level NO₂ using full residual deep networks. *Remote Sens. Environ.* 254, 112257.
- Li, T., Wang, Y., Yuan, Q., 2020. Remote sensing estimation of regional NO₂ via space-time neural networks. *Remote Sens.* 12, 2514.
- Lin, C.-A., Chen, Y.-C., Liu, C.-Y., Chen, W.-T., Seinfeld, J.H., Chou, C.C.K., 2019. Satellite-derived correlation of SO₂, NO₂, and aerosol optical depth with meteorological conditions over East Asia from 2005 to 2015. *Remote Sens.* 11, 1738.
- Liu, L., Zhang, X., Xu, W., Liu, X., Lu, X., Chen, D., Zhang, X., Wang, S., Zhang, W., 2017. Estimation of monthly bulk nitrate deposition in China based on satellite NO₂ measurement by the Ozone Monitoring Instrument. *Remote Sens. Environ.* 199, 93–106.
- Liu, Y., Ming, T., Peng, C., Wu, Y., Li, W., De Richter, R., Zhou, N., 2021. Mitigating air pollution strategies based on solar chimneys. *Sol. Energy* 218, 11–27.
- Mackerron, G., Mourato, S., 2009. Life satisfaction and air quality in London. *Ecol. Econ.* 68, 1441–1453.
- Meng, L., Liu, J., Tarasick David, W., Randel William, J., Steiner Andrea, K., Wilhelmsen, H., Wang, L., Haimberger, L., 2021. Continuous rise of the tropopause in the Northern Hemisphere over 1980–2020. *Sci. Adv.* 7, eabi8065.
- Newell, K., Kartsonaki, C., Lam, K.B.H., Kurmi, O.P., 2017. Cardiorespiratory health effects of particulate ambient air pollution exposure in low-income and middle-income countries: a systematic review and meta-analysis. *Lancet Planet. Health* 1, e368–e380.
- Nickolay, K., Lok, L., Sergey, M., Edward, C., Eric, B., William, S., Joanna, J., the OMI core team, 2019. OMI/Aura NO₂ Total and Tropospheric Column Daily L2 Global Gridded 0.25 degree x 0.25 degree V3. In: N.G.S.F. Center (Ed.): Goddard Earth Sciences Data and Information Services Center (GES DISC).
- Ogen, Y., 2020. Assessing nitrogen dioxide (NO₂) levels as a contributing factor to coronavirus (COVID-19) fatality. *Sci. Total Environ.* 726, 138605.
- OMI Team, 2012. Ozone Monitoring Instrument (OMI) data user's guide. In..
- Orellano, P., Reynoso, J., Quaranta, N., Bardach, A., Ciapponi, A., 2020. Short-term exposure to particulate matter (PM10 and PM2.5), nitrogen dioxide (NO₂), and ozone (O₃) and all-cause and cause-specific mortality: Systematic review and meta-analysis. *Environ. Int.* 142, 105876.
- Pebesma, E.J., 2004. Multivariable geostatistics in S: the gstat package. *Comput. Geosci.* 30, 683–691.
- Qin, K., Rao, L., Xu, J., Bai, Y., Zou, J., Hao, N., Li, S., Yu, C., 2017. Estimating ground level NO₂ concentrations over central-Eastern China using a satellite-based geographically and temporally weighted regression model. *Remote Sens.* 9, 950.
- Rice, M.B., Ljungman, P.L., Wilker, E.H., Gold, D.R., Schwartz, J.D., Koutrakis, P., Washko, G.R., O'Connor, G.T., Mittleman, M.A., 2013. Short-term exposure to air

- pollution and lung function in the Framingham Heart Study. *Am. J. Respir. Crit. Care Med.* 188, 1351–1357.
- Schoeberl, M.R., Douglass, A.R., Hilsenrath, E., Bhartia, P.K., Beer, R., Waters, J.W., Gunson, M.R., Froidevaux, L., Gille, J.C., Barnett, J.J., Levelt, P.F., Decola, P., 2006. Overview of the EOS aura mission. *IEEE Trans. Geosci. Remote Sens.* 44, 1066–1074.
- Shen, Y., Jiang, F., Feng, S., Zheng, Y., Cai, Z., Lyu, X., 2021. Impact of weather and emission changes on NO₂ concentrations in China during 2014–2019. *Environ. Pollut.* 269, 116163.
- Taylor, R., 1990. Interpretation of the correlation coefficient: a basic review. *J. Diagnostic Med. Sonogr.* 6, 35–39.
- Wang, B., Chen, Z., 2013. An intercomparison of satellite-derived ground-level NO₂ concentrations with GMSMB modeling results and in-situ measurements – a North American study. *Environ. Pollut.* 181, 172–181.
- Wu, X., Nethery, R.C., Sabath, M.B., Braun, D., Dominici, F., 2020. Air pollution and COVID-19 mortality in the United States: strengths and limitations of an ecological regression analysis. *Sci. Adv.* 6, eabd4049.
- Xiang, Y., Zhang, T., Liu, J., Lv, L., Dong, Y., Chen, Z., 2019. Atmosphere boundary layer height and its effect on air pollutants in Beijing during winter heavy pollution. *Atmos. Res.* 215, 305–316.
- Yao, Y., Pan, J., Liu, Z., Meng, X., Wang, W., Kan, H., Wang, W., 2021. Ambient nitrogen dioxide pollution and spreadability of COVID-19 in Chinese cities. *Ecotoxicol. Environ. Saf.* 208, 111421.
- Yousefian, F., Faridi, S., Azimi, F., Aghaei, M., Shamsipour, M., Yaghmaeian, K., Hassanvand, M.S., 2020. Temporal variations of ambient air pollutants and meteorological influences on their concentrations in Tehran during 2012–2017. *Sci. Rep.* 10, 292.
- Yu, D., Zhang, Y., Wu, X., Li, D., Li, G., 2021. The varying effects of accessing high-speed rail system on China's county development: A geographically weighted panel regression analysis. *Land Use Policy* 100, 104935.
- Zhao, Zhou, Li, Cao, He, Yu, Li, Elvidge, Cheng, Zhou, 2019. Applications of Satellite Remote Sensing of Nighttime Light Observations: Advances, Challenges, and Perspectives. *Remote Sens.* 11, 1971.
- Zheng, Yang, Wu, Marinello, 2019. Spatial Variation of NO₂ and Its Impact Factors in China: An Application of Sentinel-5P Products. *Remote Sens.* 11, 1939.